



Measurement of antiproton production from antihyperon decays in $p\text{He}$ collisions at $\sqrt{s_{\text{NN}}} = 110 \text{ GeV}$

LHCb collaboration[†]

Abstract

The interpretation of cosmic antiproton flux measurements from space-borne experiments is currently limited by the knowledge of the antiproton production cross-section in collisions between primary cosmic rays and the interstellar medium. Using collisions of protons with an energy of 6.5 TeV incident on helium nuclei at rest in the proximity of the interaction region of the LHCb experiment, the ratio of antiprotons originating from antihyperon decays to prompt production is measured for antiproton momenta between 12 and 110 GeV/ c . The dominant antihyperon contribution, namely $\bar{\Lambda} \rightarrow \bar{p}\pi^+$ decays from promptly produced $\bar{\Lambda}$ particles, is also exclusively measured. The results complement the measurement of prompt antiproton production obtained from the same data sample. At the energy scale of this measurement, the antihyperon contributions to antiproton production are observed to be significantly larger than predictions of commonly used hadronic production models.

Published in Eur. Phys. J. **C83** (2023) 543

© 2023 CERN for the benefit of the LHCb collaboration. CC BY 4.0 licence.

[†]Authors are listed at the end of this paper.

1 Introduction

In recent years, the space-borne experiments PAMELA [1] and AMS-02 [2] greatly improved measurements of the abundance of the antiproton, \bar{p} , component in cosmic rays, which is sensitive to a possible dark matter contribution [3–5]. In the 10–100 GeV \bar{p} energy range, the interpretation of their measurements requires accurate knowledge of the \bar{p} production cross-sections in the spallation of cosmic rays in the interstellar medium [6], which is mainly composed of hydrogen and helium. The LHCb experiment has the unique ability to study collisions of the LHC beams with fixed gaseous targets, including helium, reaching the 100 GeV scale for the nucleon-nucleon centre-of-mass energy, $\sqrt{s_{\text{NN}}}$, unprecedented for fixed-target experiments [7]. Using a sample of proton-helium ($p\text{He}$) collisions collected in 2016, the production of prompt antiprotons directly in the collisions or through decays of excited states was measured by the LHCb collaboration [8]. These results were the first to use a helium target, and, covering an energy scale where significant violation of Feynman scaling [9] occurs, contributed to a better modelling of the secondary \bar{p} cosmic flux [4, 10, 11].

The uncertainties on \bar{p} production from weak decays still limit the interpretation of cosmic \bar{p} data [10]. The largest of these contributions is due to antineutron decays, which cannot be directly observed in LHCb but can be estimated from the antiproton measurements and the assumption of isospin symmetry. Another significant contribution, which is less constrained theoretically, comes from decays of antihyperons, \bar{H} . Antiprotons produced in this way are referred to as *detached* in the following as they can experimentally be distinguished from prompt antiprotons in the LHCb experiment by the separation between their production vertex and the primary $p\text{He}$ collision vertex (PV).

This paper reports a determination of the ratio

$$R_{\bar{H}} \equiv \frac{\sigma(p\text{He} \rightarrow \bar{H}X \rightarrow \bar{p}X)}{\sigma(p\text{He} \rightarrow \bar{p}_{\text{prompt}}X)} \quad (1)$$

of detached to prompt antiprotons in $p\text{He}$ collisions at $\sqrt{s_{\text{NN}}} = 110$ GeV with momentum, p , ranging from 12 to 110 GeV/ c and transverse momentum, p_{T} , between 0.4 and 4 GeV/ c , where X stands for any arbitrary set of unreconstructed particles. Two approaches to the measurement, presented in Secs. 4 and 5, are followed as described below.

The dominant process, namely $\bar{\Lambda} \rightarrow \bar{p}\pi^+$ with promptly produced $\bar{\Lambda}$ particles, is measured relying only on the secondary vertex displacement from the PV and on the decay kinematics. The ratio

$$R_{\bar{\Lambda}} \equiv \frac{\sigma(p\text{He} \rightarrow \bar{\Lambda}X \rightarrow \bar{p}\pi^+X)}{\sigma(p\text{He} \rightarrow \bar{p}_{\text{prompt}}X)} \quad (2)$$

is then determined using the prompt production result [8], obtained from the same dataset.

In the second approach, an inclusive measurement of detached antiprotons is performed by exploiting the particle identification (PID) capabilities of the LHCb detector. Prompt and detached \bar{p} are distinguished by the minimum distance of their reconstructed track to the PV, the impact parameter (IP). As the relative production yields of different antihyperon states can be predicted from first principles in statistical models [12], the $R_{\bar{\Lambda}}/R_{\bar{H}}$ double ratio is expected to be predicted more reliably than the single ratios. The consistency of the two complementary approaches to the analysis is thus verified by comparing the double ratio with model predictions.

The available measurements of the $R_{\bar{\Lambda}}$ ratio, though affected by large uncertainties, hint at a significant increase of this ratio for $\sqrt{s_{\text{NN}}} > 100$ GeV [10]. The LHCb fixed-target configuration is capable of exploring the energy scale where the $R_{\bar{\Lambda}}$ enhancement occurs. The contribution to \bar{p} production from charm and beauty hadron decays is estimated to be three orders of magnitude smaller than the prompt one, using the measured $c\bar{c}$ cross-section in the same fixed-target configuration at LHCb [13] and the known charm branching fractions to baryons [14]. This is negligible compared to the accuracy of this measurement.

2 The LHCb detector and its fixed-target operation

The LHCb detector [15, 16] is a single-arm forward spectrometer covering the pseudorapidity range $2 < \eta < 5$, designed for the study of particles containing b or c quarks. The detector includes a high-precision tracking system consisting of a silicon-strip vertex detector (VELO) surrounding the proton-proton (pp) interaction region [17], a large-area silicon-strip detector located upstream of a dipole magnet with a bending power of about 4 Tm, and three stations of silicon-strip detectors and straw drift tubes [18] placed downstream of the magnet. The tracking system provides a measurement of the momentum of charged particles with a relative uncertainty that varies from 0.5% at low momentum to 1.0% at 200 GeV/ c . The IP is measured with a resolution of $(15 + 29/p_{\text{T}})$ μm , where p_{T} is measured in GeV/ c . Different types of charged hadrons are distinguished by using information from two ring-imaging Cherenkov (RICH) detectors [19], whose acceptance and performance define the \bar{p} kinematic range accessible to this study. The first RICH detector has an inner acceptance limited to $\eta < 4.4$ and is used to identify antiprotons with momenta between 12 and 60 GeV/ c . The second RICH detector, whose Cherenkov threshold for protons is 30 GeV/ c , covers the range $3 < \eta < 5$ and is used for antiproton momenta up to 110 GeV/ c . The scintillating-pad detector (SPD) of the calorimeter system is also used in this study. The SMOG (System for Measuring Overlap with Gas) system [20, 21] enables the injection of noble gases with pressure of $\mathcal{O}(10^{-7})$ mbar in the beam pipe section crossing the VELO, allowing LHCb to be operated as a fixed-target experiment. The online event selection is performed by a trigger [22], which consists of a hardware stage, requiring any activity in the SPD detector, and a software stage asking for at least one reconstructed track in the VELO. To avoid background from pp collisions, fixed-target events are acquired only when a bunch in the beam pointing toward LHCb crosses the nominal interaction region without a corresponding colliding bunch in the other beam.

3 Data sample and simulation

This measurement is performed on data specifically collected for \bar{p} production studies in May 2016. Helium gas was injected when the two beams circulating in the LHC accelerator consisted of proton bunches separated by at least 1 μs , 40 times the nominal value. In this configuration, spurious pp collisions are suppressed. A sample of $p\text{He}$ collisions with a 6.5 TeV proton-beam energy ($\sqrt{s_{\text{NN}}} = 110.5$ GeV) and corresponding to an integrated luminosity of about 0.5 nb^{-1} was collected [8]. In the proton-nucleon centre-of-mass frame, the LHCb acceptance corresponds to central and backward rapidities $-2.8 < y^* < 0.2$.

Selected events are required to have a reconstructed PV within the fiducial region $-700 < z < +100$ mm, where the z axis is along the beam direction and $z = 0$ mm corresponds to the LHCb nominal collision point in the central part of the VELO. The fiducial region is chosen to achieve a high efficiency for PV reconstruction in fixed-target collisions and a significant probability that antihyperon decays occur within the VELO. Antiproton candidates are reconstructed in the full tracking system exploiting the excellent $\bar{\Lambda}$ invariant-mass resolution and IP determination. The PV position is required to be compatible with the beam profile and events must have fewer than 5 tracks reconstructed in the VELO with negative pseudorapidity. This selection suppresses to a negligible level the background from interactions with material, decays, and particle showers produced in beam-gas collisions occurring upstream of the VELO. A sample of 33.7 million reconstructed p He collisions satisfying these requirements is obtained from the data.

Simulated data samples of p He collisions are produced with the EPOS-LHC generator [23]. The interaction of the generated particles with the detector, and its response, are implemented by using the GEANT4 toolkit [24] as described in Ref. [25]. The collisions are uniformly distributed along z in the range $-1000 < z < +300$ mm, wide enough to cover the fiducial region. When estimating efficiencies, a z -dependent weight is applied to simulated events to account for the measured gas pressure variation.

This study uses a sample of unbiased simulated inelastic collisions and several \bar{p} -enriched samples, where the simulation of the detector response is performed only if the event generated by EPOS-LHC contains a suitable \bar{p} candidate. In the sample used for the inclusive analysis, events must include at least one \bar{p} with $p_T > 0.3$ GeV/ c and $1.9 < \eta < 5.4$. In the sample used for the exclusive analysis, the antiproton must also come from a $\bar{\Lambda}$ decay occurring within the acceptance of the VELO. To study the cascade baryon contribution, a sample where the $\bar{\Lambda}$ decay follows from a $\bar{\Xi}^+ \rightarrow \bar{\Lambda}\pi^+$ decay is also simulated.

4 Exclusive $R_{\bar{\Lambda}}$ measurement

About 70% [26] of the detached antiprotons are expected to originate from decays of promptly produced $\bar{\Lambda}$ baryons and can be selected in the LHCb detector by exploiting the detached decay vertex and the invariant-mass resolution. The decay kinematics allow the antiproton to be identified from the charge and the asymmetry of the longitudinal momenta of the final-state particles with respect to the $\bar{\Lambda}$ flight direction ($p_{L\bar{\Lambda}}$),

$$\alpha_{\bar{\Lambda}} \equiv \frac{p_{L\bar{\Lambda}}(\pi^+) - p_{L\bar{\Lambda}}(\bar{p})}{p_{L\bar{\Lambda}}(\pi^+) + p_{L\bar{\Lambda}}(\bar{p})}, \quad (3)$$

which is always negative for $\bar{\Lambda}$ decays [27]. Therefore, the RICH detectors are not used in this approach. In order to minimise systematic uncertainties in the measurement of $R_{\bar{\Lambda}}$, the selection follows as much as possible that used for the prompt measurement [8]. In particular, the same fiducial volume, where the PV reconstruction efficiency cancels in the ratio, and the same kinematic region for the \bar{p} candidate, $12 < p < 110$ GeV/ c and $0.4 < p_T < 4$ GeV/ c , are required. The analysis is performed in intervals of p and p_T . These intervals are aligned with those used in the prompt measurement, except that some are merged to improve the statistical accuracy.

Table 1: Selection requirements for $\bar{\Lambda} \rightarrow \bar{p}\pi^+$ decays. Symbols are defined in the text.

Detector acceptance	$2 < \eta(\bar{p}) < 5$ $2 < \eta(\pi^+) < 5.5$ $2 < \eta(\bar{\Lambda}) < 5.5; p_{\text{T}}(\bar{\Lambda}) > 0.3 \text{ GeV}/c$
Decay geometry	$\text{IP}(\bar{\Lambda}) < 5 \text{ mm}; \chi_{\text{DOCA}}^2 < 10$ $\log[\chi_{\text{IP}}^2(\bar{p})] > 1; \log[\chi_{\text{IP}}^2(\pi^+)] > 2$ $\mathcal{F}_{\text{IP}} > 1.5; \mathcal{F}_{\chi_{\text{IP}}^2} > 4$
K_{S}^0 veto	$M_{p \rightarrow \pi} < 490$ or $M_{p \rightarrow \pi} > 511 \text{ MeV}/c^2$
Armenteros-Podolanski	$\left \left(\frac{\alpha_{\bar{\Lambda}} + 0.69}{0.18} \right)^2 + \left(\frac{p_{\text{T}\bar{\Lambda}}(\pi^+)}{100.4 \text{ MeV}/c} \right)^2 - 1 \right < 0.39$

4.1 Selection and invariant-mass fit

The $\bar{\Lambda}$ decay candidates are reconstructed from two oppositely charged tracks, which comprise segments in the VELO and in the downstream tracking stations, have a good fit quality and are incompatible with being produced at the PV. The two-track combinations are selected only if their distance of closest approach is compatible with zero using a χ^2 test (χ_{DOCA}^2). Following previous Λ production studies in LHCb [28], large discrimination against combinatorial background is obtained by combining the IP information of the $\bar{\Lambda}$ and the final-state particles into the linear discriminant

$$\mathcal{F}_{\text{IP}} \equiv \log \left(\frac{\text{IP}(\bar{p})}{1 \text{ mm}} \right) + \log \left(\frac{\text{IP}(\pi^+)}{1 \text{ mm}} \right) - \log \left(\frac{\text{IP}(\bar{\Lambda})}{1 \text{ mm}} \right). \quad (4)$$

To take into account the uncertainty on their measurements, a second discriminant $\mathcal{F}_{\chi_{\text{IP}}^2}$ is constructed by replacing IP in Eq. (4) with the χ_{IP}^2 variable, defined as the difference in the vertex-fit χ^2 of the PV reconstructed with and without the track(s) under consideration. To veto $K_{\text{S}}^0 \rightarrow \pi^- \pi^+$ decays, the misreconstructed invariant-mass $M_{p \rightarrow \pi}$, obtained by assigning the pion mass to both final-state particles, is required to be incompatible with the K_{S}^0 mass. Finally, a requirement on the Armenteros-Podolanski plane [27] ($\alpha_{\bar{\Lambda}}, p_{\text{T}\bar{\Lambda}}(\pi^+)$), where $p_{\text{T}\bar{\Lambda}}$ is the transverse momentum with respect to the $\bar{\Lambda}$ direction, is used. The selection requirements are listed in Table 1.

The purity of the selected sample is above 90% in the unbiased simulation. To subtract the residual background, the invariant-mass distribution of the $\bar{\Lambda}$ candidates is fitted with the sum of one Voigtian [29] and two Gaussian functions for the signal and a second-order polynomial for the background. This model, validated with simulation, takes into account the bias to the background distribution from the Armenteros-Podolanski plot requirement and is able to describe the data in all kinematic intervals. The invariant-mass distribution for selected $\bar{\Lambda} \rightarrow \bar{p}\pi^+$ candidates is shown in Fig. 1 together with a fit integrated over all p and p_{T} intervals, which results in a yield of $(50.7 \pm 0.3) \cdot 10^3 \bar{\Lambda} \rightarrow \bar{p}\pi^+$ decays.

4.2 Tracking efficiency

The yields of the selected candidates in each kinematic interval are corrected for the total reconstruction and selection efficiencies. These are determined as the ratio of signal

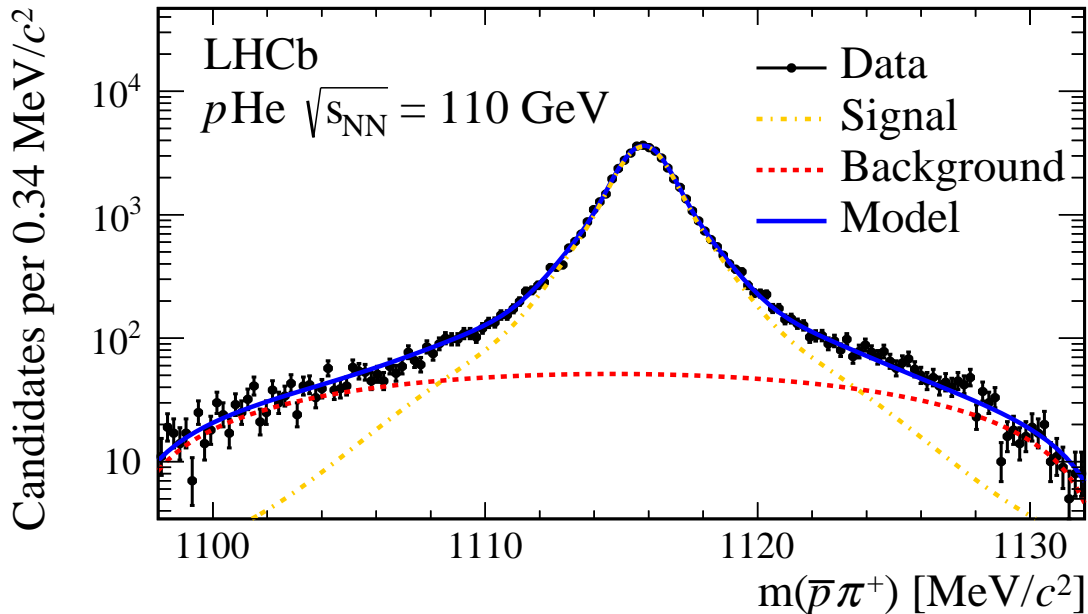


Figure 1: Invariant-mass distribution for the $\bar{\Lambda} \rightarrow \bar{p}\pi^+$ candidates selected in the $p\text{He}$ data. The fit model is overlaid on the data.

yields obtained by the invariant-mass fit of the $\bar{\Lambda}$ candidates in the \bar{p} -enriched simulated sample to the number of actual candidates generated by the EPOS-LHC model in the same interval of p and p_T . With this procedure, the efficiency takes into account the resolution effects resulting in migration across kinematic intervals. The largest inefficiency comes from decays occurring downstream of the VELO and can be accurately predicted. For the upstream decays, the average track reconstruction efficiency is determined in simulation to be $(95.84 \pm 0.04)\%$ for the antiprotons and $(85.40 \pm 0.06)\%$ for the pions, which tend to have a lower momentum. The quoted uncertainties are only due to the finite simulated sample size. These efficiencies are corrected by factors determined from calibration samples in pp data, which are consistent with unity in all kinematic intervals within their systematic uncertainty of 0.8% [30].

As illustrated in Fig. 2, the tracks considered in this study exhibit a different topology, notably in the VELO, with respect to the prompt tracks from pp collisions used for calibration, because of the larger spread of the fixed-target collision position and the long $\bar{\Lambda}$ flight distance. The validation of the VELO tracking efficiency is therefore extended using partially reconstructed $\bar{\Lambda} \rightarrow \bar{p}\pi^+$ decay candidates in the $p\text{He}$ collision sample, where the candidate \bar{p} is reconstructed in the tracking stations upstream and downstream of the magnet but ignoring the information from the VELO. To take into account the degraded resolution of the decay vertex, the selection is loosened by requiring $\mathcal{F}_{\text{IP}} > 1$ and $\mathcal{F}_{\chi^2_{\text{IP}}} > 3$, while the pion, reconstructed using the whole tracking system, is required to be identified by the RICH detectors to compensate for the larger background. The VELO tracking efficiency is estimated from the fraction of candidates in this sample where the partially reconstructed track satisfies the quality requirements for a fully reconstructed track when including the information from the VELO. The VELO efficiencies measured in data and simulation with the same analysis are compared in Fig. 3, notably as a function of the \bar{p}

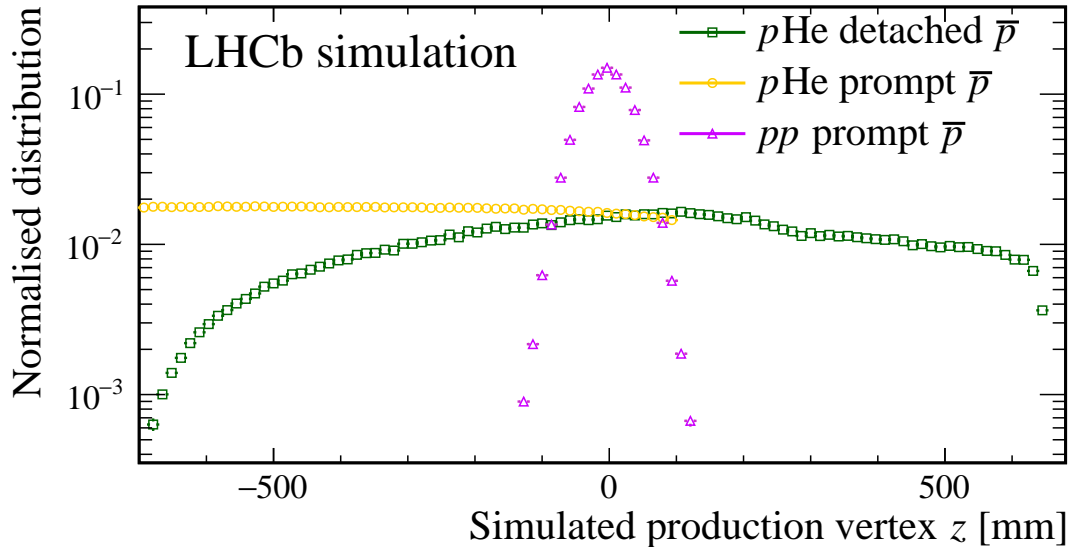


Figure 2: Normalised distributions of the production vertex z coordinate for simulated prompt and detached \bar{p} in $p\text{He}$ collisions and for prompt \bar{p} in simulated pp collisions in the kinematic range explored in this paper. The PV fiducial region for $p\text{He}$ collisions is $-700 < z < 100$ mm.

production vertex position. No significant differences are observed. The uncertainty on the \bar{p} reconstruction efficiency in each kinematic interval is expected to cancel in the $R_{\bar{\Lambda}}$ ratio. Therefore, a 0.8% systematic uncertainty on $R_{\bar{\Lambda}}$ from the π^+ tracking efficiency is assigned.

4.3 Other systematic uncertainties

A fit model uncertainty is evaluated by repeating the fit with an additional Gaussian component in the signal model or with an Argus function [31] for the background model. In both cases, the variation of the result is smaller than the statistical uncertainty in both data and simulation. The online selection requirements are found to be fully efficient in a control sample with randomly selected events. Each of the offline selection requirements listed in Table 1 has an efficiency larger than 90%, with a total selection efficiency of 70%. The largest inefficiencies are attributed to the requirements on \mathcal{F}_{IP} , $\mathcal{F}_{\chi^2_{\text{IP}}}$ and $M_{p \rightarrow \pi}$. The normalised distributions of the two \mathcal{F} discriminants are compared between data and simulated signal. The background contamination is statistically subtracted from the data by modelling the $\bar{\Lambda}$ invariant-mass distributions and by applying the *sPlot* technique [32] with $m(\bar{p}\pi^+)$ as discriminating variable. The efficiencies of the requirements in Table 1 are measured on the resulting distributions and the difference between data and simulation, amounting to 1%, is assigned as systematic uncertainty. As a further cross-check of the reliability of the simulation in the wide fiducial region for fixed-target collisions, the analysis is repeated in four equally populated intervals of the PV z position. The efficiency-corrected signal yields are found to agree within the statistical uncertainties. To check that the \bar{p} -enriched simulated sample does not bias the efficiency estimation, a simulated sample with a looser $\bar{\Lambda}$ selection is used. The total signal efficiencies are found to agree in all kinematic intervals.

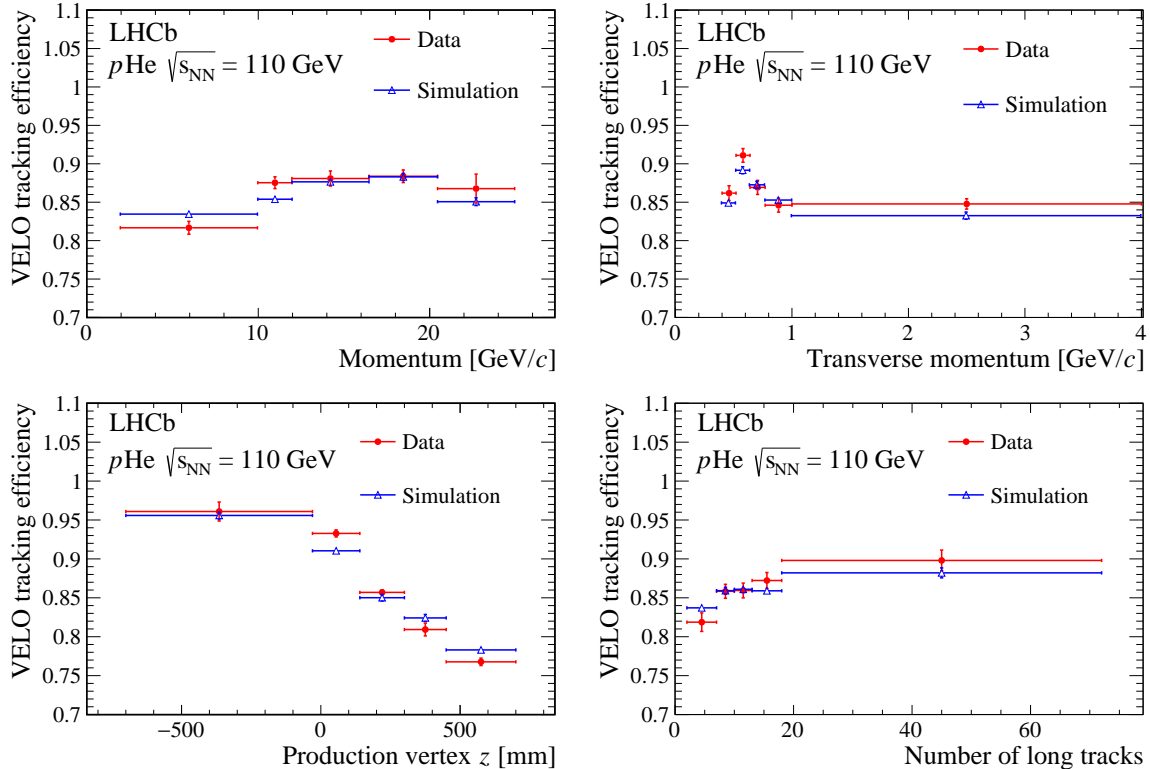


Figure 3: VELO tracking efficiency for \bar{p} in $\bar{\Lambda} \rightarrow \bar{p}\pi^+$ decays as a function of (top left) the particle momentum, (top right) the transverse momentum, (bottom left) the production vertex z coordinate and (bottom right) the number of reconstructed long tracks in the event.

4.4 Results

The ratio $R_{\bar{\Lambda}}$ is determined in each kinematic interval from the measured yield $N_{\bar{\Lambda}}$ of $\bar{\Lambda} \rightarrow \bar{p}\pi^+$ decays, the total efficiency $\epsilon_{\bar{\Lambda}}$ and the corresponding quantities for prompt \bar{p} production [8] as

$$R_{\bar{\Lambda}} = \frac{N_{\bar{\Lambda}} \epsilon_{\bar{p}}}{N_{\bar{p}} \epsilon_{\bar{\Lambda}}}. \quad (5)$$

The $N_{\bar{\Lambda}}$ yields determined from the fits to the $\bar{\Lambda}$ invariant-mass distributions are corrected by 0.6% to account for the contribution from collisions on the residual gas of the LHC vacuum contaminating the helium target, as estimated in Ref. [8]. The related uncertainty is expected to cancel in the ratio. All significant sources of systematic uncertainty on the $R_{\bar{\Lambda}}$ ratio are listed in Table 2. The leading contributions relate to the particle identification of prompt antiprotons and to the limited size of the produced $\bar{\Lambda}$ sample. The $R_{\bar{\Lambda}}$ results are illustrated in Fig. 4 and reported in Appendix A for the kinematic intervals that are common to this and the prompt antiproton production analysis. The results as a function of p (p_{T}), integrated over the $0.55 < p_{\text{T}} < 1.2 \text{ GeV}/c$ ($12 < p < 50.5 \text{ GeV}/c$) region, are shown in Fig. 5 and compared to widely used hadronic collision models included in the CRMC package [26]. The data indicate that all considered generators significantly underestimate the $\bar{\Lambda}$ contribution to the \bar{p} production.

Table 2: Relative uncertainties on the $R_{\bar{\Lambda}}$ measurement.

Particle identification ($N_{\bar{p}}$)	0% – 36% (< 5% for most intervals)
Statistical uncertainty ($N_{\bar{\Lambda}}$)	2.2% – 11% (< 4% for most intervals)
Statistical uncertainty ($N_{\bar{p}}$)	0.5% – 11% (< 2% for most intervals)
Simulated sample size ($\epsilon_{\bar{\Lambda}}$)	1.8% – 4.1% (< 2% for most intervals)
Simulated sample size ($\epsilon_{\bar{p}}$)	0.4% – 11% (< 2% for most intervals)
Background subtraction ($N_{\bar{p}}$)	1.1%
Selection efficiency ($\epsilon_{\bar{\Lambda}}$)	1%
Tracking efficiency for π^+ ($\epsilon_{\bar{\Lambda}}$)	0.8%

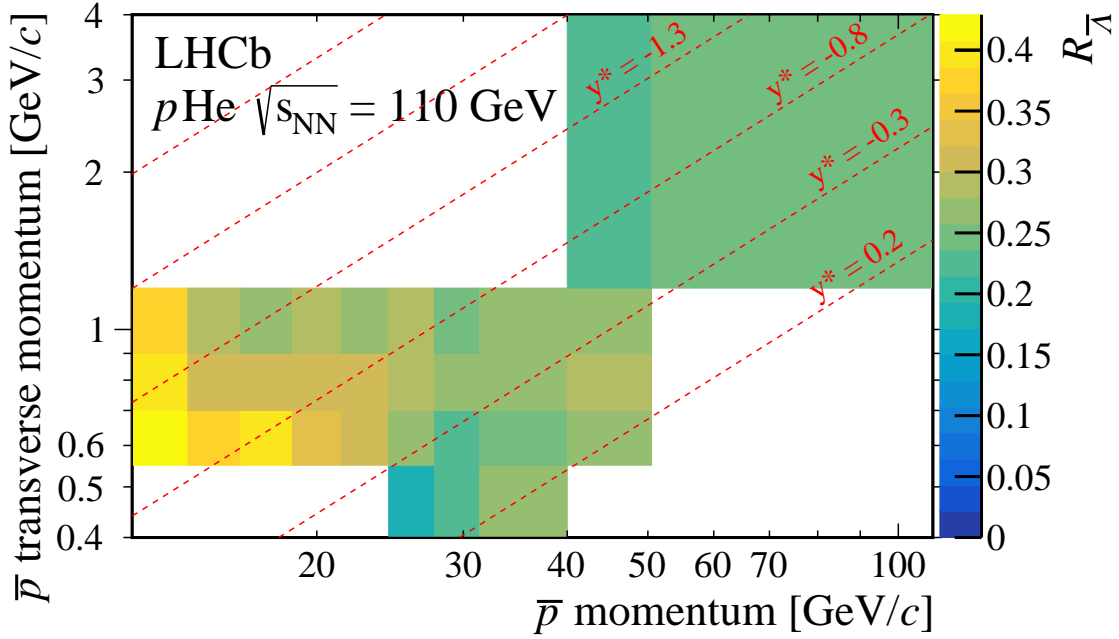


Figure 4: Measured $R_{\bar{\Lambda}}$ in each of the considered p and p_T intervals.

5 Inclusive $R_{\bar{H}}$ measurement

An alternative inclusive approach to the measurement of the detached \bar{p} yield relies on the PID capabilities of the RICH detectors and on the IP resolution of the VELO, rather than on the reconstruction of the \bar{H} decays. In this second analysis, a high-purity \bar{p} sample is selected through a tight PID requirement. Prompt and detached antiprotons are statistically resolved through a template fit to the distribution of the χ_{IP}^2 variable. Figure 6 shows the $\log(\chi_{\text{IP}}^2)$ distribution for all simulated \bar{p} in the \bar{p} -enriched sample. Three contributions can be clearly distinguished, mainly corresponding to prompt, detached, and antiprotons produced in secondary collisions with the detector material. A non-Gaussian tail of the prompt distribution, extending towards the detached \bar{p} region, is attributed to scattering in the material separating the primary LHC vacuum and the VELO, as further discussed in Section 5.2. Antiproton candidates are selected from negatively charged tracks reconstructed with a high-quality fit including segments in the VELO and in the tracking stations upstream and downstream of the magnet. The analysis is

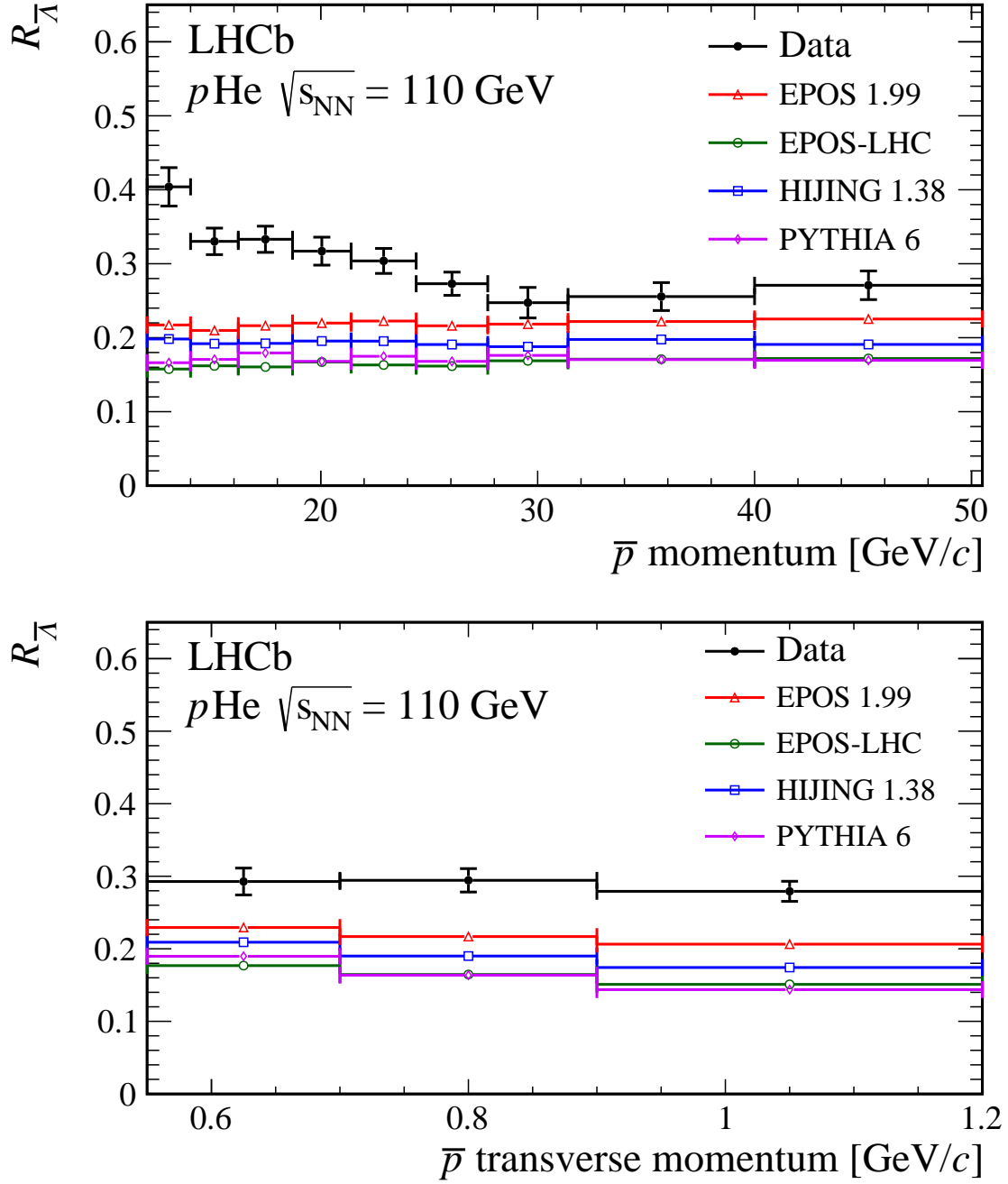


Figure 5: Measured $R_{\bar{\Lambda}}$ as a function of (top) the \bar{p} momentum for $0.55 < p_T < 1.2$ GeV/ c and (bottom) the \bar{p} transverse momentum for $12 < p < 50.5$ GeV/ c . The measurement is compared to the predictions, in the same kinematic regions, from the EPOS 1.99 [33], EPOS-LHC [23], HIJING 1.38 [34] and PYTHIA 6 [35] models, included in the CRMC package [26]. Error bars on data represent the total uncertainty.

performed in the (p, p_T) plane, with ten momentum intervals between 12 and 110 GeV/ c and five for p_T between 0.4 and 4 GeV/ c . The \bar{p} identification is based on two quantities determined from the response of the RICH detectors: the difference between the logarithm of the likelihood of the proton and pion hypotheses, $DLL_{p\pi}$, and that between the proton

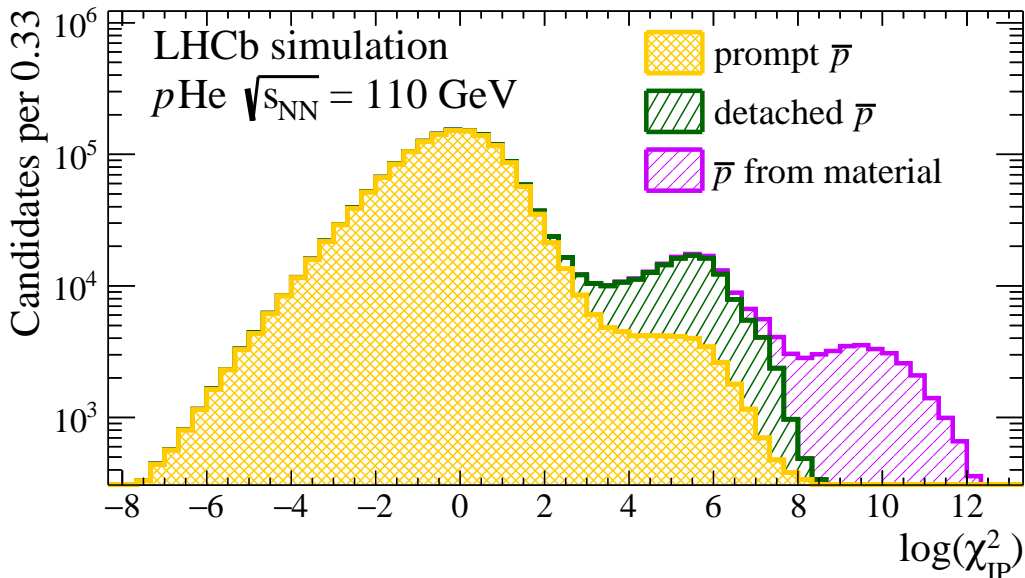


Figure 6: Distributions of the $\log(\chi_{\text{IP}}^2)$ variable for all simulated antiprotons in the \bar{p} -enriched simulated sample. The contributions from prompt, detached and antiprotons produced in the detector material are separately shown.

and kaon hypotheses, DLL_{pK} [19]. A tight selection is used, requiring $\text{DLL}_{p\pi} > 20$ and $\text{DLL}_{pK} > 10$, to suppress contamination from misidentified particles. Kinematic intervals at the boundaries of the RICH capabilities, where the \bar{p} purity predicted in simulation is below 80%, are removed from the analysis. The overall predicted purity of the resulting \bar{p} sample is 97%. The numbers of reconstructed prompt and detached \bar{p} , N_{prompt} and N_{det} , are determined from the fit and then corrected for the corresponding efficiencies as estimated from simulation. These are then used to calculate

$$R_{\bar{H}} = \frac{N_{\text{det}}}{N_{\text{prompt}}} \frac{\epsilon_{\text{prompt}}}{\epsilon_{\text{det}}}. \quad (6)$$

Efficiencies are determined from the simulation as the ratio between the number of selected candidates in each interval of reconstructed p and p_{T} , and the number generated by the EPOS-LHC model in the same kinematic interval.

5.1 Template fit

Templates for the χ_{IP}^2 distributions are drawn from the \bar{p} -enriched simulation in each kinematic interval for different categories of candidates: three templates for the prompt, detached and secondary \bar{p} and four templates for misidentified particles, consisting of pions, kaons, electrons and fake tracks. Smoothed curves are obtained through a parametrisation of the probability density functions as a sum of Gaussian functions, whose parameters are obtained from a fit to the simulated event distributions, as illustrated in Fig. 7. For each template the number of Gaussian components, whose parameters are initialized to random values in the appropriate range, is increased, up to 15, until a good fit is obtained.

The template fits are performed with the fractions of the three \bar{p} components left free to float, while the small contributions from misidentified particles are fixed to the values

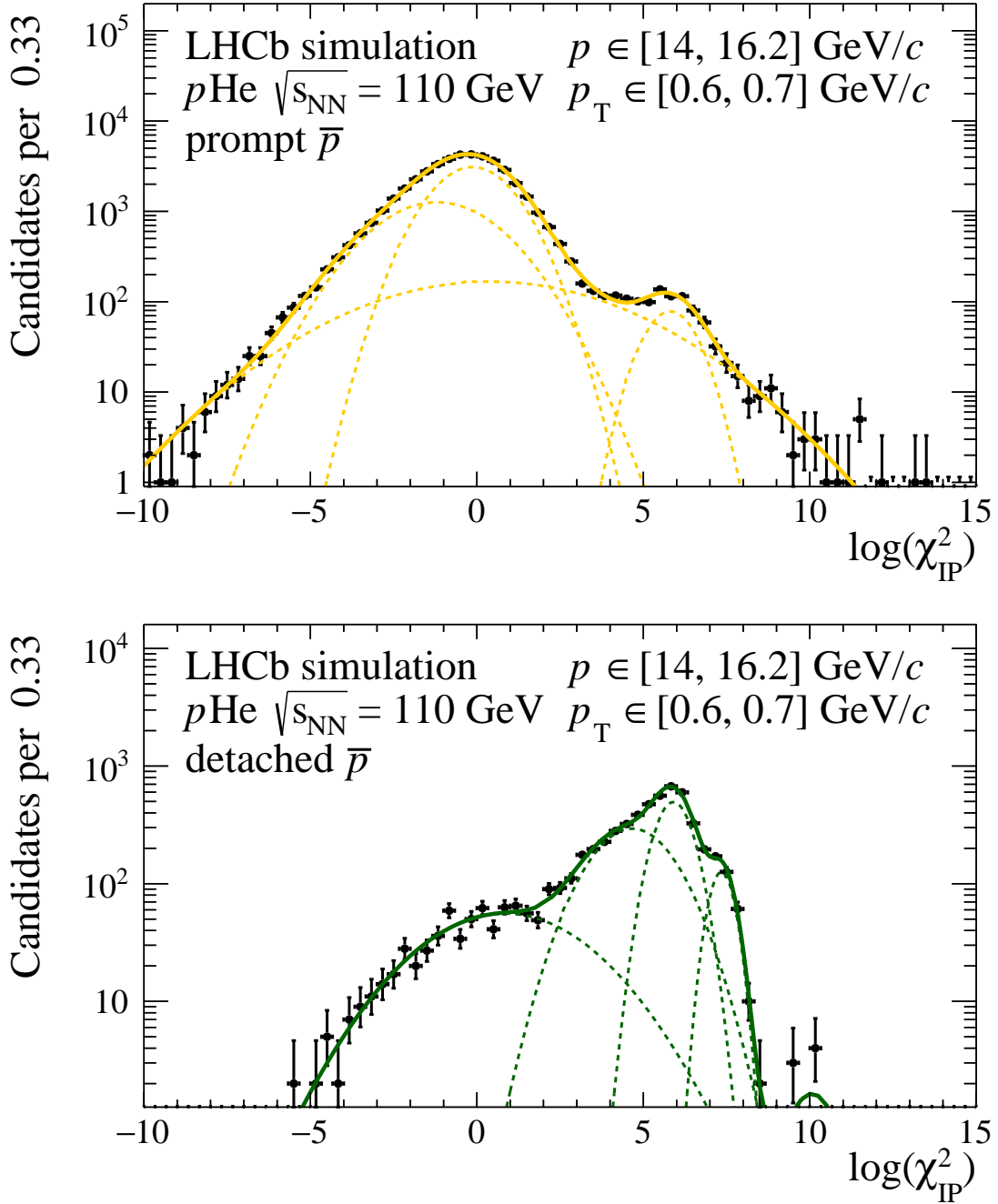


Figure 7: Distributions of $\log(\chi_{\text{IP}}^2)$ for (top) prompt and (bottom) detached antiprotons in the \bar{p} -enriched simulated sample for a kinematic interval in the central region of the considered phase-space. The fit model is overlaid on the data.

predicted by the unbiased simulation. The procedure is validated by performing the fit to the unbiased simulated sample and verifying that the obtained abundance for each of the three \bar{p} categories agrees with the actual value within the statistical uncertainties. The fit is then applied to the data. Figure 8 shows the fit result integrated over all kinematic intervals. The raw ratio of detached to prompt reconstructed candidates is found to be $R_{\text{raw}} \equiv N_{\text{det}}/N_{\text{prompt}} = 0.1247 \pm 0.0005$, where the uncertainty is statistical

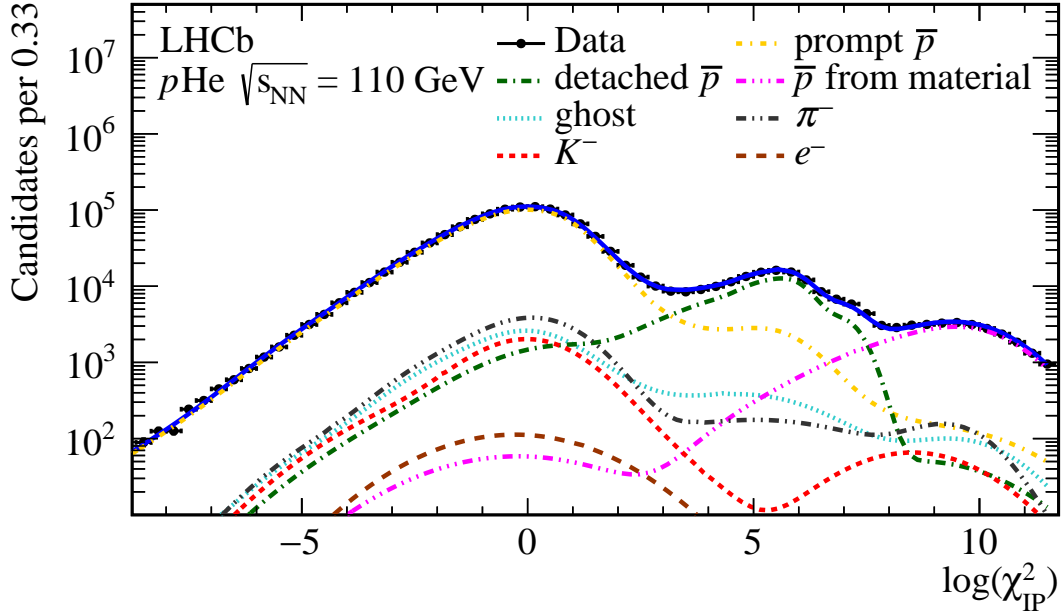


Figure 8: Distributions of the $\log(\chi_{\text{IP}}^2)$ variable in the data sample integrated over all kinematic intervals. The fit model is overlaid on the data.

only. This is significantly larger than the value predicted by the unbiased simulated sample, 0.0848 ± 0.0014 , confirming a sizeable underestimation of the antihyperon component by the EPOS-LHC generator.

5.2 Scattered prompt antiprotons

Figure 6 shows that a significant fraction of simulated prompt \bar{p} candidates are reconstructed with an IP value well above the expected resolution, compatible with the detached \bar{p} typical values. As illustrated in Fig. 9, this is due to scattering that may change the track trajectory of the prompt \bar{p} when the particle crosses the aluminium foil, shown in Fig. 10, separating the primary LHC vacuum from the VELO sensor volume. The tail is indeed found to be strongly dependent on the azimuthal angle ϕ . The simulation of the material geometry and of the scattering cross-section is therefore critical to the determination of $R_{\bar{H}}$. A validation using data of the predicted prompt \bar{p} template is performed by selecting $\bar{\Lambda}(1520) \rightarrow \bar{p}K^+$ decays. These happen at the primary interaction vertex and, tagged by the invariant-mass of the parent particle and by the kaon identification, provide a prompt \bar{p} sample in data. Since a small sample size of these decays is selected in the $p\text{He}$ collision sample, the analysis is performed on the largest fixed-target sample collected during the LHC Run 2, namely a sample of proton-neon ($p\text{Ne}$) collisions with beam energy of 2.5 TeV acquired in 2017. The \bar{p} candidate is selected with the same requirements as for the inclusive study, while the tagging kaon must satisfy $\text{DLL}_{K\pi} \equiv \text{DLL}_{p\pi} - \text{DLL}_{pK} > 20$, $\text{DLL}_{pK} < 0$ and $\log(\chi_{\text{IP}}^2) < 3$ to enforce prompt decays. Events are weighted according to the \bar{p} transverse momentum and the SPD hit multiplicity to equalize these distributions with those observed for the prompt \bar{p} candidates in $p\text{He}$ data. The $\bar{\Lambda}(1520) \rightarrow \bar{p}K^+$ yield is determined in intervals of the \bar{p} $\log(\chi_{\text{IP}}^2)$. The background is

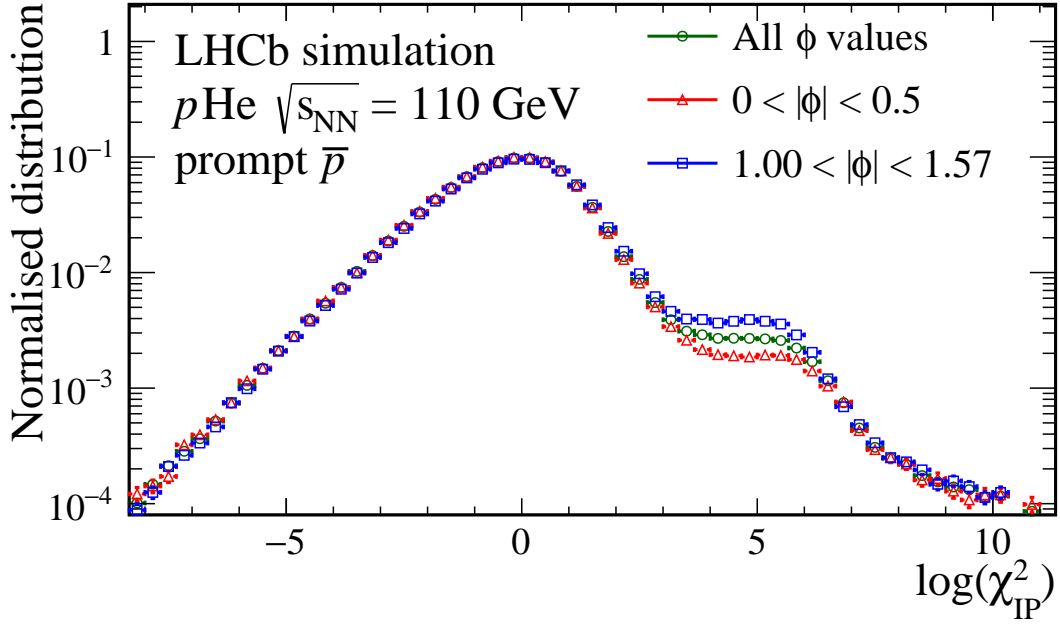


Figure 9: Normalised distributions of the prompt $\bar{p} \log(\chi_{\text{IP}}^2)$ variable in different ranges of the azimuthal angle $\phi = \text{atan}(p_y/p_x)$.

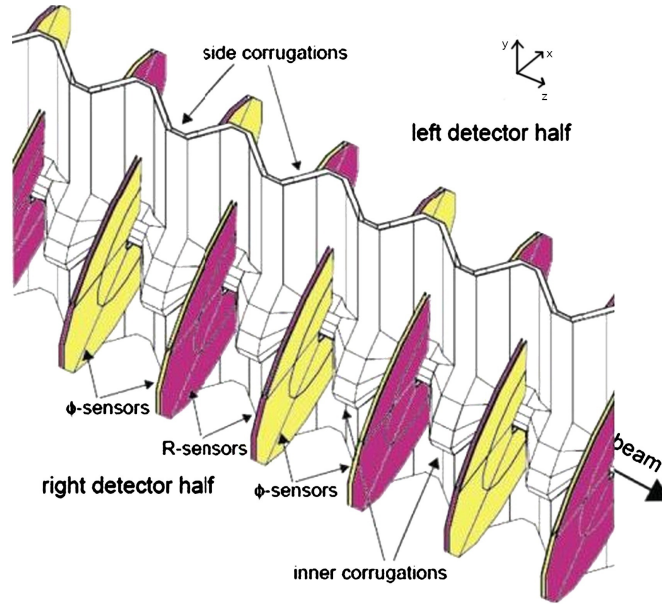


Figure 10: Sketch of the VELO [36], where the aluminium foils crossed by the particles before entering the VELO volume is visible. The crossed material is maximum for $|\phi| > 1$.

subtracted by fitting the $\bar{p}K^+$ invariant-mass distribution with a Voigtian function for the signal and an exponential function for the background, as illustrated in Fig. 11. The fit parameter representing the signal mass resolution in each interval is independent, as it degrades for increasing values of χ_{IP}^2 . Figure 12 shows the resulting reconstructed $\log(\chi_{\text{IP}}^2)$ distribution for the prompt \bar{p} candidates. A reasonable agreement with the template

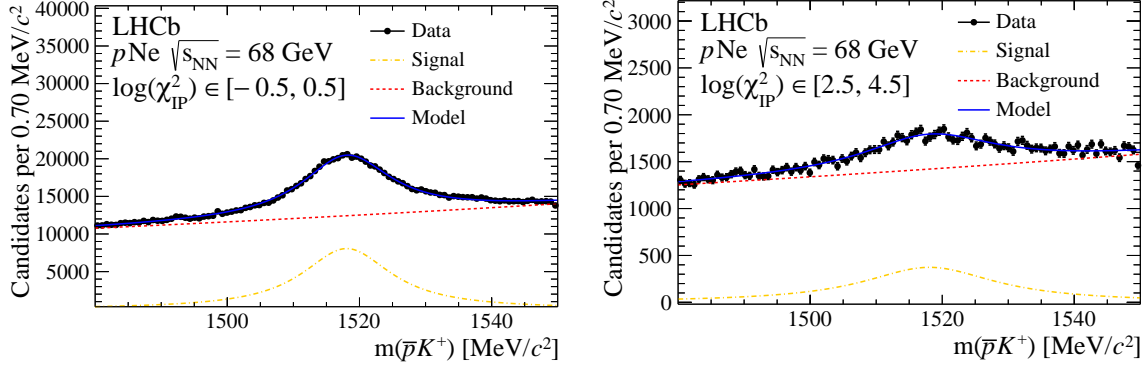


Figure 11: Invariant-mass distributions for the $\bar{\Lambda}(1520) \rightarrow \bar{p}K^+$ candidates selected in the $p\text{Ne}$ data within two intervals of the $\bar{p} \log(\chi_{\text{IP}}^2)$ variable. The fit model is overlaid on the data.

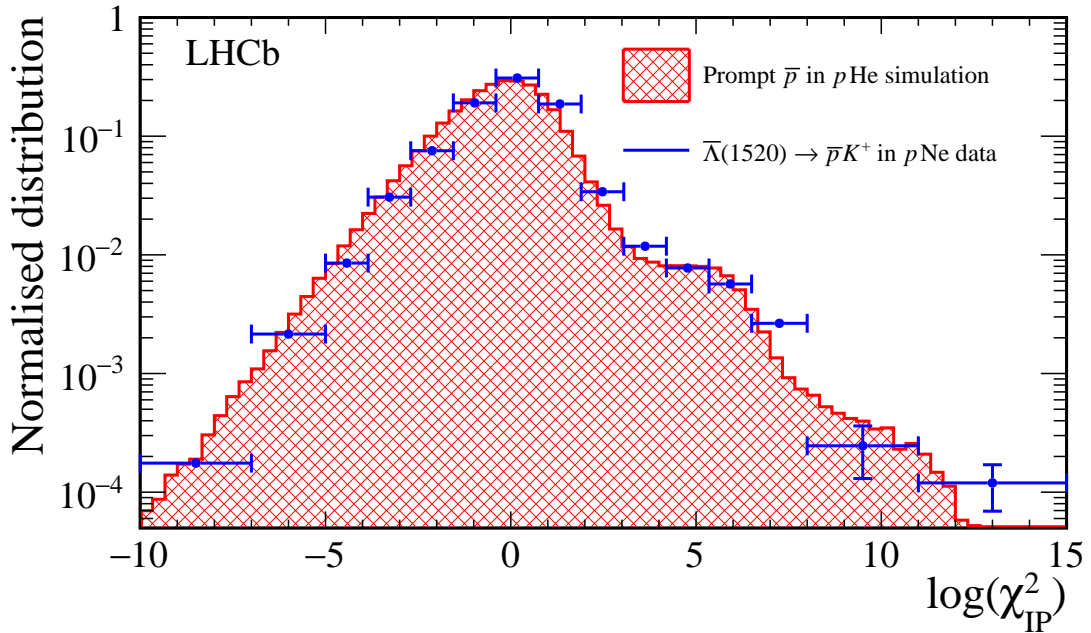


Figure 12: Distributions of the number of signal candidates determined in each interval of the antiproton $\log(\chi_{\text{IP}}^2)$ compared to the prediction of the $p\text{He}$ simulation for selected prompt antiprotons.

from simulation is found, though differences are expected due to the simplification of the material geometry in the simulation. To estimate the related systematic uncertainty, the inclusive template fit for the sample integrated over all intervals is repeated using this template drawn using data for the prompt \bar{p} component. The relative variation of R_{raw} is 4.8% and is assigned as systematic uncertainty.

5.3 Antihyperon decays

The detached \bar{p} efficiency, in particular the fraction of \bar{H} decays occurring within the VELO, strongly depends on the assumed relative production yields of the different antihyperons

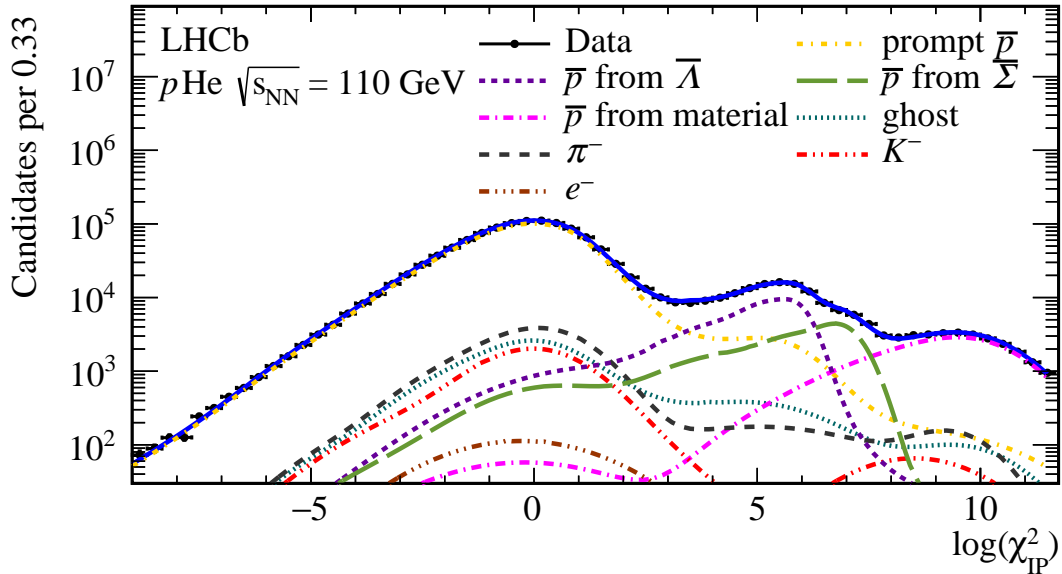


Figure 13: Distribution of the $\log(\chi_{\text{IP}}^2)$ variable in the data sample integrated over all kinematic intervals modelled with independent components for $\bar{\Sigma}^-$ decays (labelled as \bar{p} from $\bar{\Sigma}^-$) and all other antihyperon decays (\bar{p} from $\bar{\Lambda}$).

contributing to the inclusive \bar{p} yield. The EPOS-LHC model predicts that, in the measured kinematic range, 72% of the \bar{p} candidates originate from $\bar{\Lambda} \rightarrow \bar{p}\pi^+$ decays of promptly produced $\bar{\Lambda}$ particles, 17% from $\bar{\Sigma}^- \rightarrow \bar{p}\pi^0$ decays, 11% from $\bar{\Xi}^+ \rightarrow \bar{\Lambda}\pi^+$ and $\bar{\Xi}^0 \rightarrow \bar{\Lambda}\pi^0$ cascade decays, and less than 1% from $\bar{\Omega}^+$ decays. These predictions are expected to be accurate within a relative uncertainty of approximately 20% [12]. The assumed values of $\bar{\Sigma}^-/\bar{H}$ and $\bar{\Xi}^+/\bar{\Lambda}$ ratios are verified with the collision data.

The template fit is expected to have sensitivity to the contribution of $\bar{\Sigma}^-$ decays, as illustrated in Fig. 13. Indeed, when compared to $\bar{\Lambda}$ decays, the $\bar{\Sigma}^- \rightarrow \bar{p}\pi^0$ decay Q-value is larger and antiprotons show on average a larger IP. The fit is repeated with two independent detached \bar{p} components: the $\bar{\Sigma}^-$ decays and all other decays. The best fit fraction of $\bar{\Sigma}^-$ is larger than the EPOS-LHC prediction by a factor 1.13 ± 0.02 . This correction factor, compatible with the expected theoretical uncertainty, is applied to the simulated sample to recompute the efficiency and correct the detached \bar{p} templates. While the fit results for R_{raw} change less than 1%, the variation of ϵ_{det} implies a change to $R_{\bar{H}}$ between 1.2% and 3.8%, depending on the kinematic interval. This is assigned as a systematic uncertainty on $R_{\bar{H}}$ due to the relative $\bar{\Sigma}^-$ production.

To check the cascade contribution, the $\bar{\Xi}^+ \rightarrow \bar{\Lambda}\pi^+$ yield is directly measured and compared to the $\bar{\Lambda} \rightarrow \bar{p}\pi^+$ one. Candidates are selected combining a reconstructed $\bar{\Lambda}$ decay with a π^+ candidate track with a distance of closest approach to the $\bar{\Lambda}$ trajectory compatible with zero. Similarly to the prompt $\bar{\Lambda}$ selection, prompt $\bar{\Xi}^+$ decays are selected using a linear discriminant: $\log[\chi_{\text{IP}}^2(\bar{\Lambda})] + \log[\chi_{\text{IP}}^2(\pi^+)] - \log[\chi_{\text{IP}}^2(\bar{\Xi}^+)] > 0$. To minimise the systematic bias in the $\bar{\Xi}^+/\bar{\Lambda}$ ratio, the final-state $\bar{\Lambda}$ selection follows the same requirements as the prompt $\bar{\Lambda}$ candidates, except that on χ_{IP}^2 , and a loose selection is chosen for the π^+ candidate, without any PID requirement. The z distribution of the decays is also

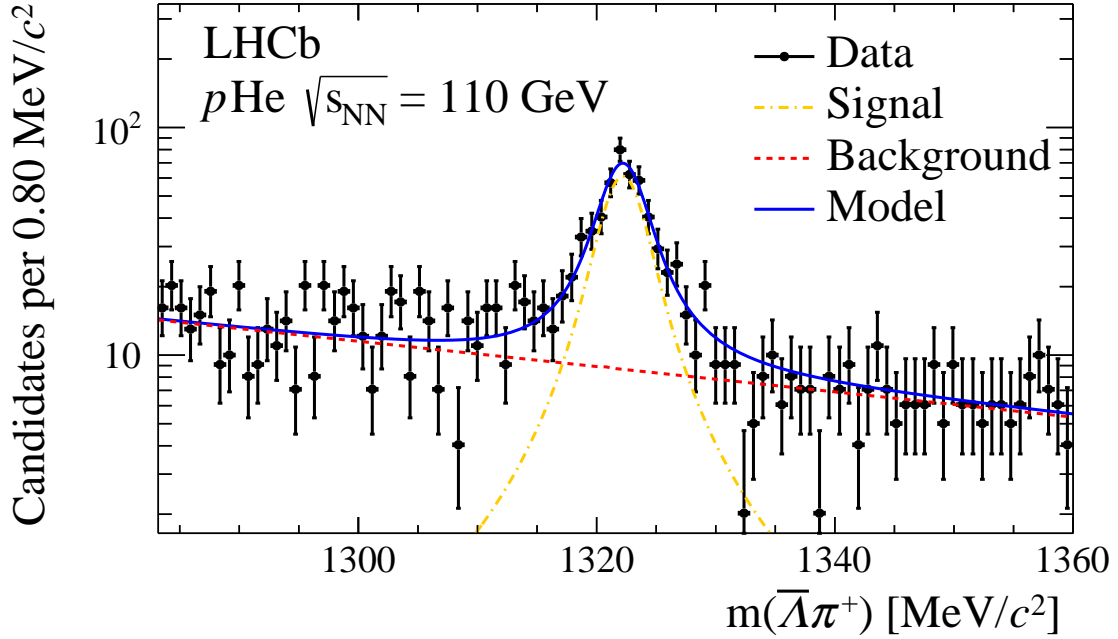


Figure 14: Invariant-mass distribution for the $\Xi^+ \rightarrow \bar{\Lambda}\pi^+$ candidates selected in the $p\text{He}$ data. The fit model is overlaid on the data.

equalised, by weighting the prompt $\bar{\Lambda}$ candidates to reproduce the observed distribution of $\bar{\Lambda}$ decay vertices from the reconstructed Ξ^+ decays. The invariant-mass distribution of the $\Xi^+ \rightarrow \bar{\Lambda}\pi^+$ candidates is displayed in Fig. 14, where the fit to determine the signal yield is also shown. The fit model, verified on simulation, uses a Voigtian function for the signal and an exponential function for the background. The same analysis is performed on the simulated sample and the yield ratio $\sigma(\Xi^+)/\sigma(\bar{\Lambda})$ is found to be larger in data with respect to the EPOS-LHC model by a factor 1.09 ± 0.09 . This factor is used to weight the relative production yield of both Ξ^+ and Ξ^0 baryons in the simulation when deriving the detached \bar{p} templates in the nominal fits. The related uncertainty corresponds to a systematic uncertainty on $R_{\bar{H}}$ from cascade production, varying between 0.6% and 0.9%, depending on the kinematic interval.

5.4 Other systematic uncertainties

The fit model uncertainty is estimated by repeating it with the raw binned distributions as templates and is found, in most intervals, to be below 2%.

Once the probability that antihyperon decays occur within the VELO is taken into account, the reconstruction and selection efficiencies are expected to mostly cancel in the $R_{\bar{H}}$ ratio. Residual differences are still expected from the different distributions of the production vertex position due to the decaying antihyperons flight distance. The overall tracking efficiency is measured in the simulation as $(94.85 \pm 0.01)\%$ for prompt and $(93.47 \pm 0.05)\%$ for detached antiprotons, with the quoted uncertainties due to the finite simulated sample size. The small difference is mainly due to the lower average number of hits in the VELO for the latter. As discussed in Section 4.2, these geometrical effects are

Table 3: Relative uncertainties on the $R_{\bar{H}}$ measurement.

Prompt \bar{p} template		4.8%
Statistical uncertainty	1.9% – 6.2% (< 2.5% for most intervals)	
Template parametrisation	0 – 5.3% (< 2% for most intervals)	
Simulated sample size	1.5% – 5.8% (< 1.8% for most intervals)	
Production of $\bar{\Sigma}^-$		1.2 – 3.8%
Particle identification		0.9%
Production of $\bar{\Xi}$		0.6 – 0.9%
Gas z profile simulation	0.1 – 1.5% (< 0.5% for most intervals)	

verified to be predicted reliably and no significant systematic uncertainty is assumed.

A larger bias could be induced by the tight PID selection. In the simulation, its efficiency is measured to be $(64.90 \pm 0.03)\%$ and $(57.74 \pm 0.11)\%$ for prompt and detached antiprotons, respectively. The quoted uncertainties correspond to the finite simulated sample size. These predictions are validated using high-purity \bar{p} samples from $\bar{\Lambda} \rightarrow \bar{p}\pi^+$ decays, where the antiproton is identified without using the RICH. A large sample of these decays is selected from the p Ne collision sample acquired in 2017. A machine-learning-based approach, documented in Ref. [37], is used to model the PID response as a function of 12 variables related to the particle trajectory, its reconstruction quality and the event occupancy. This model, applied to the simulated events, is able to reproduce the predicted PID efficiency for the two \bar{p} categories within the statistical uncertainties, which are lower than 1%. This demonstrates that the predicted difference is due to geometrical effects and that the RICH response for a given track topology and detector occupancy is accurately simulated. On the other hand, the RICH detector response is affected by low-energy background that is not accurately simulated. For the selected $\bar{\Lambda} \rightarrow \bar{p}\pi^+$ decays in the p He sample, the distributions of RICH hit multiplicities differ from those predicted in simulation, and the efficiency of the PID requirement is found to be larger by a relative 8% than the predicted value. To check for the sensitivity of the results to the PID selection thresholds, the PID efficiency correction is recomputed in simulation after loosening the selection to reproduce the efficiency measured in data for the detached component. The $R_{\bar{H}}$ value changes by 0.9%, which is assigned as the systematic uncertainty on the PID selection. The systematic uncertainties on the predicted fraction of misidentified particles is also evaluated from this check and its effect on $R_{\bar{H}}$ is found to be negligible.

A systematic uncertainty on the assumed longitudinal profile of the gas target density is assigned from the change of the $\varepsilon_{\text{det}}/\varepsilon_{\text{prompt}}$ ratio when introducing the weights to equalize the PV z distribution in data and simulation. It amounts to less than 0.5% in most kinematic intervals.

5.5 Results

The results for each kinematic interval are illustrated in Fig. 15 and the numerical values are provided in Appendix A. Table 3 summarises the uncertainties in the $R_{\bar{H}}$ measurement. The inclusive results as a function of p or p_T , integrated in the other variable, are shown in Fig. 16. As already observed in the $R_{\bar{\Lambda}}$ measurement, the most commonly used hadronic collision generators are shown to underestimate the antihyperon contribution to

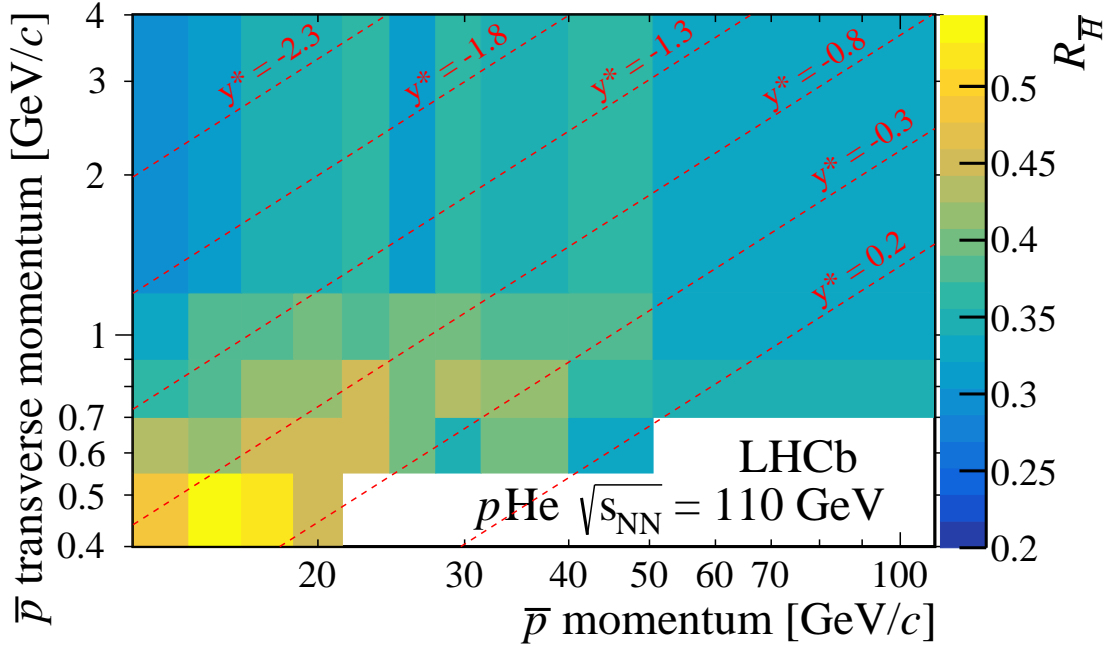


Figure 15: Measured $R_{\bar{H}}$ in each of the considered p and p_T intervals.

\bar{p} production at $\sqrt{s_{\text{NN}}} = 110$ GeV.

The ratio $R_{\bar{\Lambda}}/R_{\bar{H}}$ measured with the inclusive and exclusive approaches is compared with the EPOS-LHC prediction in Fig. 17. As this ratio is predicted more reliably than the inclusive detached \bar{p} yield, the good agreement between the measured and predicted values provides a mutual validation for the results of the two complementary approaches followed in this paper.

6 Conclusions

In conclusion, the production of antiprotons from antihyperon decays relative to the prompt \bar{p} production is measured in the fixed-target configuration of the LHCb experiment from $p\text{He}$ collisions at $\sqrt{s_{\text{NN}}} = 110$ GeV. The results confirm previous findings from colliders [39–41] for an increased \bar{H} contribution with respect to the $\sqrt{s_{\text{NN}}} \sim 10$ GeV scale probed in past fixed-target experiments and indicate a sizeable underestimation of this contribution in most hadronic production models used in cosmic ray physics. A significant dependence of $R_{\bar{H}}$ on the \bar{p} momentum is observed. This effect is not usually considered in the modelling of the secondary \bar{p} component in cosmic rays, where $R_{\bar{H}}$ is assumed to depend only on $\sqrt{s_{\text{NN}}}$ [10, 11]. These results are thus expected to provide a valuable input to improve the predictions for the secondary \bar{p} cosmic flux.

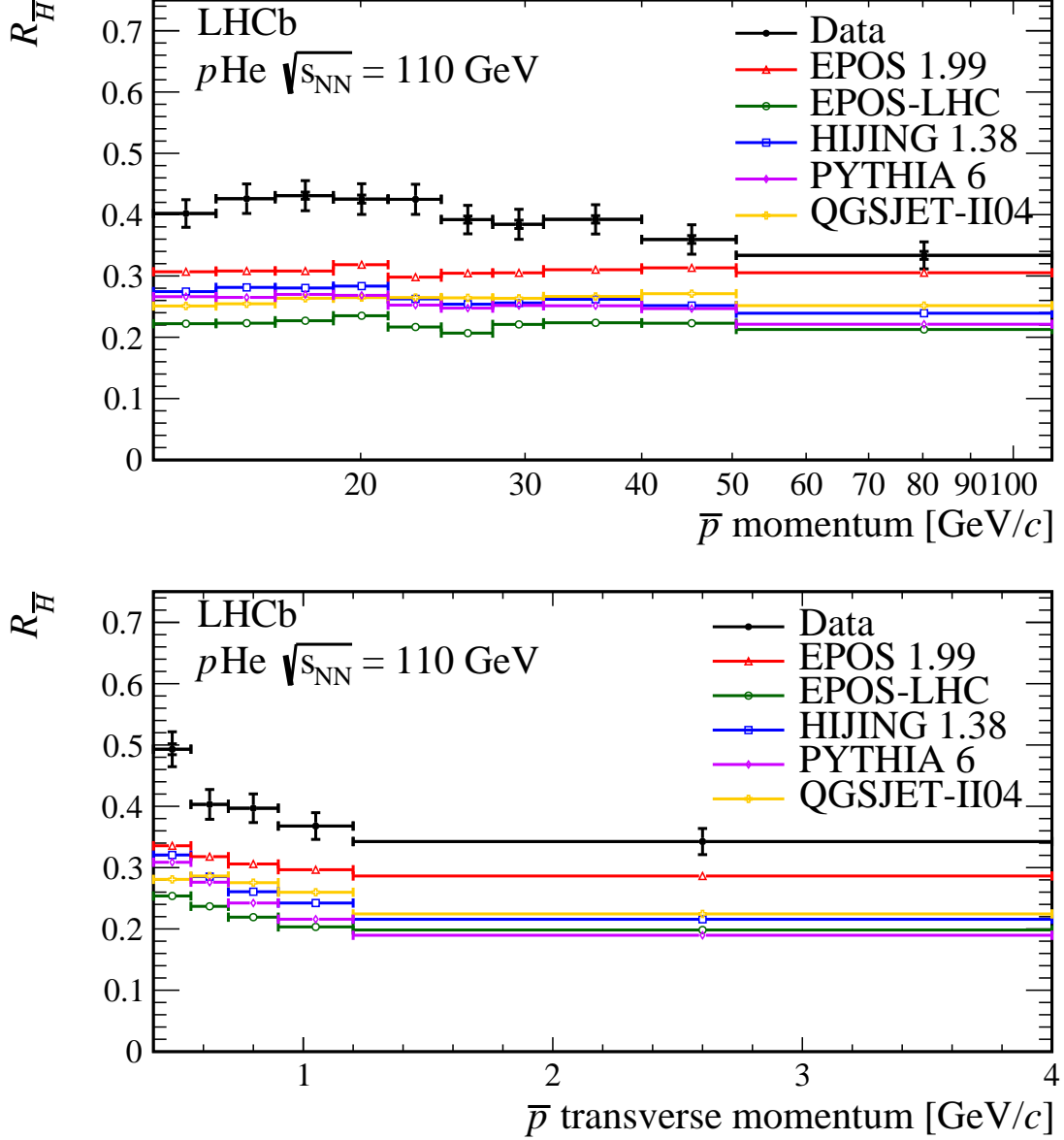


Figure 16: Measured $R_{\bar{H}}$ as a function of (top) the \bar{p} momentum for $0.4 < p_{\text{T}} < 4$ GeV/ c and (bottom) the \bar{p} transverse momentum for $12 < p < 110$ GeV/ c . The measurement is compared to predictions, in the same kinematic regions, from the EPOS 1.99 [33], EPOS-LHC [23], HIJING 1.38 [34], PYTHIA 6 [35] and QGSJET-II04 [38] models, included in the CRMC package [26]. Error bars on data represent the total uncertainty.

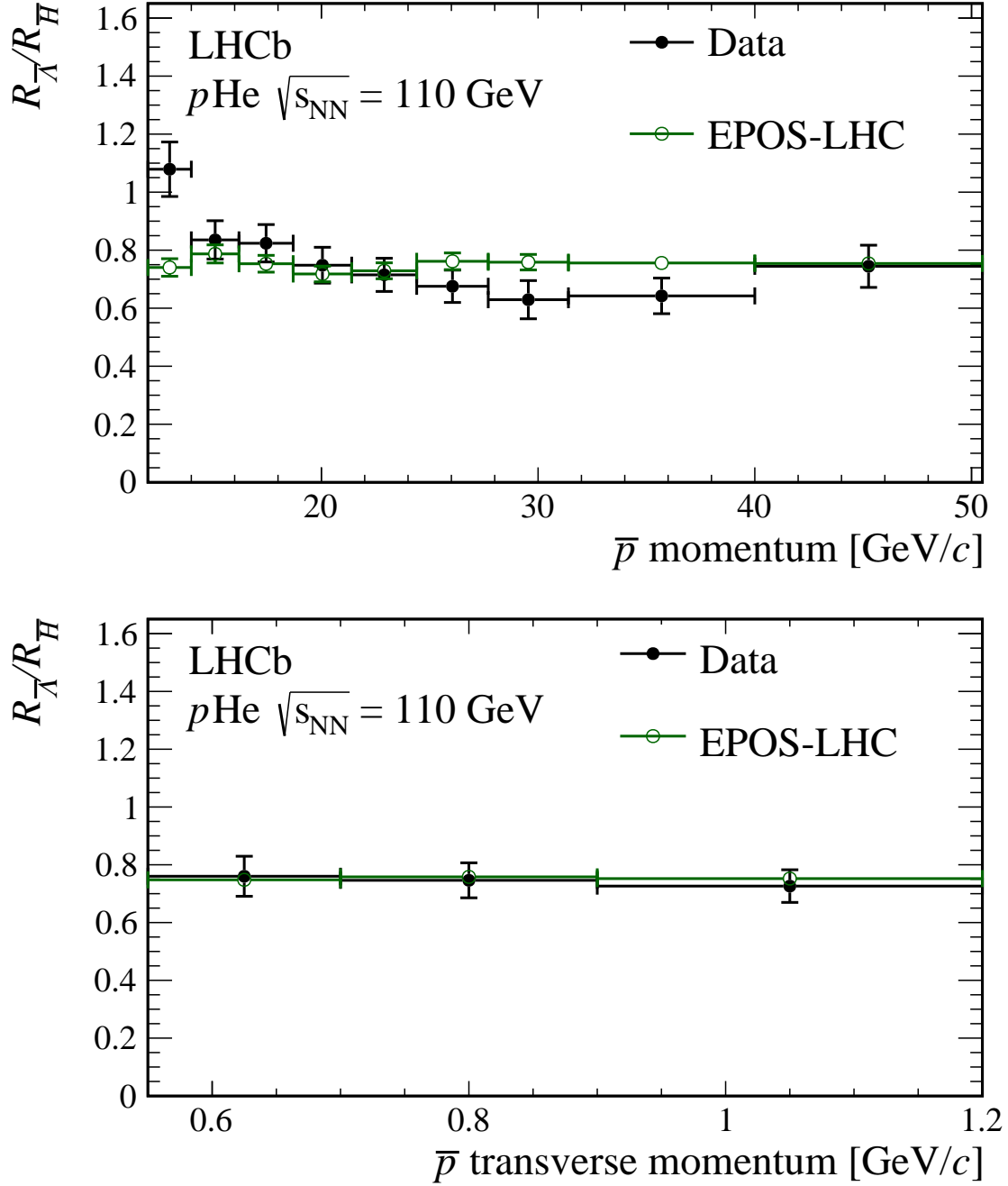


Figure 17: Fraction of antiprotons from decays of promptly produced $\bar{\Lambda}$ particles to the total yield of detached antiprotons as a function of (top) their momentum for $0.55 < p_T < 1.2$ GeV/ c and (bottom) their transverse momentum for $12 < p < 50.5$ GeV/ c . The data are compared to the EPOS-LHC [23] prediction for this quantity. Error bars on data represent the total uncertainty.

Acknowledgements

We express our gratitude to our colleagues in the CERN accelerator departments for the excellent performance of the LHC. We thank the technical and administrative staff at the LHCb institutes. We acknowledge support from CERN and from the national agencies: CAPES, CNPq, FAPERJ and FINEP (Brazil); MOST and NSFC (China); CNRS/IN2P3 (France); BMBF, DFG and MPG (Germany); INFN (Italy); NWO (Netherlands); MNiSW and NCN (Poland); MEN/IFA (Romania); MICINN (Spain); SNSF and SER (Switzerland); NASU (Ukraine); STFC (United Kingdom); DOE NP and NSF (USA). We acknowledge the computing resources that are provided by CERN, IN2P3 (France), KIT and DESY (Germany), INFN (Italy), SURF (Netherlands), PIC (Spain), GridPP (United Kingdom), CSCS (Switzerland), IFIN-HH (Romania), CBPF (Brazil), Polish WLCG (Poland) and NERSC (USA). We are indebted to the communities behind the multiple open-source software packages on which we depend. Individual groups or members have received support from ARC and ARDC (Australia); Minciencias (Colombia); AvH Foundation (Germany); EPLANET, Marie Skłodowska-Curie Actions and ERC (European Union); A*MIDEX, ANR, IPhU and Labex P2IO, and Région Auvergne-Rhône-Alpes (France); Key Research Program of Frontier Sciences of CAS, CAS PIFI, CAS CCEPP, Fundamental Research Funds for the Central Universities, and Sci. & Tech. Program of Guangzhou (China); GVA, XuntaGal, GENCAT and Prog. Atracción Talento, CM (Spain); SRC (Sweden); the Leverhulme Trust, the Royal Society and UKRI (United Kingdom).

A Numerical results

The numerical results for the measurements of the $R_{\bar{\Lambda}}$ and $R_{\bar{H}}$ ratios, presented in Secs. 4 and 5, are reported in Table 4 in intervals of the antiproton momentum and transverse momentum.

Table 4: Measured $R_{\bar{H}}$ and $R_{\bar{\Lambda}}$ ratios in intervals of the antiproton momentum and transverse momentum, measured in GeV/ c units. The average momentum and transverse momentum, as predicted by the EPOS-LHC generator for prompt antiprotons, are also listed for each interval in GeV/ c units. The uncertainty is split into an uncorrelated component, denoted with δ_{uncorr} , and a component that is fully correlated among the kinematic intervals, denoted δ_{corr} .

p^{min}	$\langle p \rangle$	p^{max}	$p_{\text{T}}^{\text{min}}$	$\langle p_{\text{T}} \rangle$	$p_{\text{T}}^{\text{max}}$	$R_{\bar{H}}$	δ_{uncorr}	δ_{corr}	$R_{\bar{\Lambda}}$	δ_{uncorr}	δ_{corr}
12.0	12.98	14.0	0.40	0.47	0.55	0.477	0.013	0.025	—	—	—
12.0	12.99	14.0	0.55	0.62	0.70	0.433	0.012	0.023	0.429	0.019	0.022
12.0	12.99	14.0	0.70	0.79	0.90	0.371	0.012	0.020	0.395	0.036	0.019
12.0	12.99	14.0	0.90	1.02	1.20	0.337	0.016	0.019	0.377	0.042	0.013
12.0	13.00	14.0	1.20	1.47	4.00	0.303	0.026	0.018	—	—	—
14.0	15.08	16.2	0.40	0.47	0.55	0.546	0.018	0.029	—	—	—
14.0	15.09	16.2	0.55	0.62	0.70	0.423	0.011	0.022	0.370	0.017	0.019
14.0	15.09	16.2	0.70	0.79	0.90	0.387	0.010	0.021	0.317	0.012	0.016
14.0	15.09	16.2	0.90	1.02	1.20	0.383	0.014	0.022	0.290	0.018	0.011
14.0	15.10	16.2	1.20	1.48	4.00	0.311	0.022	0.019	—	—	—
16.2	17.43	18.7	0.40	0.47	0.55	0.518	0.022	0.027	—	—	—
16.2	17.43	18.7	0.55	0.62	0.70	0.442	0.012	0.024	0.395	0.018	0.019
16.2	17.43	18.7	0.70	0.79	0.90	0.412	0.010	0.022	0.317	0.012	0.016
16.2	17.44	18.7	0.90	1.02	1.20	0.374	0.012	0.021	0.273	0.015	0.011
16.2	17.44	18.7	1.20	1.49	4.00	0.352	0.020	0.020	—	—	—
18.7	20.03	21.4	0.40	0.47	0.55	0.447	0.024	0.025	—	—	—
18.7	20.03	21.4	0.55	0.62	0.70	0.458	0.013	0.024	0.342	0.028	0.017
18.7	20.03	21.4	0.70	0.79	0.90	0.417	0.010	0.023	0.320	0.014	0.016
18.7	20.04	21.4	0.90	1.03	1.20	0.406	0.012	0.023	0.280	0.014	0.011
18.7	20.05	21.4	1.20	1.49	4.00	0.344	0.017	0.021	—	—	—
21.4	22.88	24.4	0.55	0.62	0.70	0.456	0.015	0.025	0.316	0.015	0.015
21.4	22.89	24.4	0.70	0.79	0.90	0.446	0.011	0.024	0.312	0.013	0.015
21.4	22.88	24.4	0.90	1.03	1.20	0.382	0.011	0.022	0.277	0.023	0.011
21.4	22.89	24.4	1.20	1.50	4.00	0.370	0.017	0.022	—	—	—
24.4	26.02	27.7	0.40	0.47	0.55	—	—	—	0.180	0.065	0.009
24.4	26.02	27.7	0.55	0.62	0.70	0.400	0.016	0.022	0.260	0.016	0.013
24.4	26.02	27.7	0.70	0.79	0.90	0.407	0.011	0.023	0.283	0.015	0.013
24.4	26.03	27.7	0.90	1.03	1.20	0.405	0.012	0.023	0.280	0.016	0.011
24.4	26.04	27.7	1.20	1.51	4.00	0.321	0.014	0.019	—	—	—

p^{\min}	$\langle p \rangle$	p^{\max}	p_{T}^{\min}	$\langle p_{\text{T}} \rangle$	p_{T}^{\min}	$R_{\bar{H}}$	δ_{uncorr}	δ_{corr}	$R_{\bar{A}}$	δ_{uncorr}	δ_{corr}
27.7	29.52	31.4	0.40	0.47	0.55	—	—	—	0.226	0.059	0.011
27.7	29.52	31.4	0.55	0.62	0.70	0.349	0.019	0.023	0.224	0.034	0.011
27.7	29.53	31.4	0.70	0.79	0.90	0.430	0.014	0.024	0.273	0.012	0.014
27.7	29.53	31.4	0.90	1.03	1.20	0.394	0.012	0.023	0.253	0.011	0.010
27.7	29.53	31.4	1.20	1.52	4.00	0.357	0.015	0.021	—	—	—
31.4	35.55	40.0	0.40	0.47	0.55	—	—	—	0.279	0.050	0.017
31.4	35.56	40.0	0.55	0.62	0.70	0.398	0.017	0.023	0.247	0.032	0.013
31.4	35.57	40.0	0.70	0.79	0.90	0.412	0.013	0.024	0.257	0.012	0.014
31.4	35.58	40.0	0.90	1.03	1.20	0.385	0.010	0.022	0.268	0.009	0.009
31.4	35.60	40.0	1.20	1.52	4.00	0.350	0.010	0.021	—	—	—
40.0	45.08	50.5	0.55	0.62	0.70	0.326	0.019	0.025	0.261	0.016	0.015
40.0	45.08	50.5	0.70	0.79	0.90	0.362	0.014	0.022	0.280	0.014	0.016
40.0	45.08	50.5	0.90	1.03	1.20	0.382	0.013	0.023	0.272	0.037	0.012
40.0	45.12	50.5	1.20	1.54	4.00	0.364	0.012	0.022	0.229	0.011	0.005
50.5	76.35	110.0	0.70	0.79	0.90	0.351	0.021	0.025	—	—	—
50.5	76.50	110.0	0.90	1.03	1.20	0.323	0.013	0.019	—	—	—
50.5	76.97	110.0	1.20	1.55	4.00	0.336	0.010	0.020	0.244	0.010	0.012

References

- [1] PAMELA collaboration, O. Adriani *et al.*, *New measurement of the antiproton-to-proton flux ratio up to 100 GeV in the cosmic radiation*, Phys. Rev. Lett. **102** (2009) 051101, [arXiv:0810.4994](#).
- [2] AMS collaboration, M. Aguilar *et al.*, *The Alpha Magnetic Spectrometer (AMS) on the international space station: Part II — Results from the first seven years*, Phys. Rept. **894** (2021) 1.
- [3] A. Reinert and M. W. Winkler, *A precision search for WIMPs with charged cosmic rays*, JCAP **01** (2018) 055, [arXiv:1712.00002](#).
- [4] M. Boudaud *et al.*, *AMS-02 antiprotons' consistency with a secondary astrophysical origin*, Phys. Rev. Res. **2** (2020) 023022, [arXiv:1906.07119](#).
- [5] A. Cuoco *et al.*, *Scrutinizing the evidence for dark matter in cosmic-ray antiprotons*, Phys. Rev. **D99** (2019) 103014, [arXiv:1903.01472](#).
- [6] G. Giesen *et al.*, *AMS-02 antiprotons, at last! secondary astrophysical component and immediate implications for dark matter*, JCAP **09** (2015) 023, [arXiv:1504.04276](#).
- [7] A. Bursche *et al.*, *Physics opportunities with the fixed-target program of the LHCb experiment using an unpolarized gas target*, LHCb-PUB-2018-015, 2018.
- [8] LHCb collaboration, R. Aaij *et al.*, *Measurement of antiproton production in pHe collisions at $\sqrt{s_{\text{NN}}} = 110$ GeV*, Phys. Rev. Lett. **121** (2018) 222001, [arXiv:1808.06127](#).

- [9] R. P. Feynman, *Very high-energy collisions of hadrons*, Phys. Rev. Lett. **23** (1969) 1415.
- [10] M. W. Winkler, *Cosmic ray antiprotons at high energies*, JCAP **02** (2017) 048, arXiv:1701.04866.
- [11] M. Korsmeier, F. Donato, and M. Di Mauro, *Production cross sections of cosmic antiprotons in the light of new data from the NA61 and LHCb experiments*, Phys. Rev. **D97** (2018) 103019, arXiv:1802.03030.
- [12] F. Becattini, P. Castorina, A. Milov, and H. Satz, *A Comparative analysis of statistical hadron production*, Eur. Phys. J. **C66** (2010) 377, arXiv:0911.3026.
- [13] LHCb collaboration, R. Aaij *et al.*, *First measurement of charm production in fixed-target configuration at the LHC*, Phys. Rev. Lett. **122** (2019) 132002, arXiv:1810.07907.
- [14] L. Gladilin, *Fragmentation fractions of c and b quarks into charmed hadrons at LEP*, Eur. Phys. J. **C75** (2015) 19, arXiv:1404.3888.
- [15] LHCb collaboration, A. A. Alves Jr. *et al.*, *The LHCb detector at the LHC*, JINST **3** (2008) S08005.
- [16] LHCb collaboration, R. Aaij *et al.*, *LHCb detector performance*, Int. J. Mod. Phys. **A30** (2015) 1530022, arXiv:1412.6352.
- [17] R. Aaij *et al.*, *Performance of the LHCb Vertex Locator*, JINST **9** (2014) P09007, arXiv:1405.7808.
- [18] P. d'Argent *et al.*, *Improved performance of the LHCb Outer Tracker in LHC Run 2*, JINST **12** (2017) P11016, arXiv:1708.00819.
- [19] M. Adinolfi *et al.*, *Performance of the LHCb RICH detector at the LHC*, Eur. Phys. J. **C73** (2013) 2431, arXiv:1211.6759.
- [20] C. Barschel, *Precision luminosity measurement at LHCb with beam-gas imaging*, CERN-THESIS-2013-301, 2014, Ph.D. thesis, RWTH Aachen U.
- [21] LHCb collaboration, R. Aaij *et al.*, *Precision luminosity measurements at LHCb*, JINST **9** (2014) P12005, arXiv:1410.0149.
- [22] R. Aaij *et al.*, *The LHCb trigger and its performance in 2011*, JINST **8** (2013) P04022, arXiv:1211.3055.
- [23] T. Pierog *et al.*, *EPOS LHC: test of collective hadronization with data measured at the CERN Large Hadron Collider*, Phys. Rev. **C92** (2015) 034906, arXiv:1306.0121.
- [24] Geant4 collaboration, J. Allison *et al.*, *Geant4 developments and applications*, IEEE Trans. Nucl. Sci. **53** (2006) 270; Geant4 collaboration, S. Agostinelli *et al.*, *Geant4: A simulation toolkit*, Nucl. Instrum. Meth. **A506** (2003) 250.
- [25] M. Clemencic *et al.*, *The LHCb simulation application, Gauss: Design, evolution and experience*, J. Phys. Conf. Ser. **331** (2011) 032023.

- [26] T. Pierog, C. Baus, and R. Ulrich, *CRMC library package, version 1.5.6.r4962*, web.ikp.kit.edu/rulrich/crmc.htm.
- [27] J. Podolanski and R. Armenteros, *Analysis of V-events*, The London, Edinburgh, and Dublin Philosophical Magazine and Journal of Science **45** (1954) 13.
- [28] LHCb collaboration, R. Aaij *et al.*, *Measurement of V^0 production ratios in pp collisions at $\sqrt{s} = 0.9$ and 7 TeV*, JHEP **08** (2011) 034, [arXiv:1107.0882](https://arxiv.org/abs/1107.0882).
- [29] J. J. Olivero and R. L. Longbothum, *Empirical fits to the voigt line width: A brief review*, Journal of Quantitative Spectroscopy and Radiative Transfer **17** (1977) 233.
- [30] LHCb collaboration, R. Aaij *et al.*, *Measurement of the track reconstruction efficiency at LHCb*, JINST **10** (2015) P02007, [arXiv:1408.1251](https://arxiv.org/abs/1408.1251).
- [31] ARGUS collaboration, H. Albrecht *et al.*, *Search for hadronic $b \rightarrow u$ decays*, Phys. Lett. **B241** (1990) 278.
- [32] M. Pivk and F. R. Le Diberder, *sPlot: A statistical tool to unfold data distributions*, Nucl. Instrum. Meth. **A555** (2005) 356, [arXiv:physics/0402083](https://arxiv.org/abs/physics/0402083).
- [33] T. Pierog and K. Werner, *EPOS model and ultra high energy cosmic rays*, Nucl. Phys. B Proc. Suppl. **196** (2009) 102, [arXiv:0905.1198](https://arxiv.org/abs/0905.1198).
- [34] M. Gyulassy and X.-N. Wang, *HIJING 1.0: A Monte Carlo program for parton and particle production in high-energy hadronic and nuclear collisions*, Comput. Phys. Commun. **83** (1994) 307, [arXiv:nuc1-th/9502021](https://arxiv.org/abs/nuc1-th/9502021).
- [35] T. Sjöstrand, S. Mrenna, and P. Skands, *PYTHIA 6.4 physics and manual*, JHEP **2006** (2006) 026.
- [36] M. T. Alexander, *LHCb VELO tracking resolutions*, Nucl. Instrum. Meth. **A699** (2013) 184.
- [37] G. Graziani *et al.*, *A neural-network-defined Gaussian mixture model for particle identification applied to the LHCb fixed-target programme*, JINST **17** (2022) P02018, [arXiv:2110.10259](https://arxiv.org/abs/2110.10259).
- [38] S. Ostapchenko, *QGSJET-II: towards reliable description of very high energy hadronic interactions*, Nucl. Phys. B Proc. Suppl. **151** (2006) 143, [arXiv:hep-ph/0412332](https://arxiv.org/abs/hep-ph/0412332).
- [39] STAR collaboration, B. I. Abelev *et al.*, *Strange particle production in p+p collisions at $\sqrt{s} = 200$ GeV*, Phys. Rev. **C75** (2007) 064901, [arXiv:nuc1-ex/0607033](https://arxiv.org/abs/nuc1-ex/0607033).
- [40] ALICE collaboration, K. Aamodt *et al.*, *Strange particle production in proton-proton collisions at $\sqrt{s} = 0.9$ TeV with ALICE at the LHC*, Eur. Phys. J. **C71** (2011) 1594, [arXiv:1012.3257](https://arxiv.org/abs/1012.3257).
- [41] CMS collaboration, V. Khachatryan *et al.*, *Strange particle production in pp collisions at $\sqrt{s} = 0.9$ and 7 TeV*, JHEP **05** (2011) 064, [arXiv:1102.4282](https://arxiv.org/abs/1102.4282).

V. Zhukov^{14,38} , Q. Zou^{4,6} , S. Zucchelli^{20,9} , D. Zuliani²⁸ , G. Zunica⁵⁶ .

- ¹ *Centro Brasileiro de Pesquisas Físicas (CBPF), Rio de Janeiro, Brazil*
- ² *Universidade Federal do Rio de Janeiro (UFRJ), Rio de Janeiro, Brazil*
- ³ *Center for High Energy Physics, Tsinghua University, Beijing, China*
- ⁴ *Institute Of High Energy Physics (IHEP), Beijing, China*
- ⁵ *School of Physics State Key Laboratory of Nuclear Physics and Technology, Peking University, Beijing, China*
- ⁶ *University of Chinese Academy of Sciences, Beijing, China*
- ⁷ *Institute of Particle Physics, Central China Normal University, Wuhan, Hubei, China*
- ⁸ *Université Savoie Mont Blanc, CNRS, IN2P3-LAPP, Annecy, France*
- ⁹ *Université Clermont Auvergne, CNRS/IN2P3, LPC, Clermont-Ferrand, France*
- ¹⁰ *Aix Marseille Univ, CNRS/IN2P3, CPPM, Marseille, France*
- ¹¹ *Université Paris-Saclay, CNRS/IN2P3, IJCLab, Orsay, France*
- ¹² *Laboratoire Leprince-Ringuet, CNRS/IN2P3, Ecole Polytechnique, Institut Polytechnique de Paris, Palaiseau, France*
- ¹³ *LPNHE, Sorbonne Université, Paris Diderot Sorbonne Paris Cité, CNRS/IN2P3, Paris, France*
- ¹⁴ *I. Physikalisches Institut, RWTH Aachen University, Aachen, Germany*
- ¹⁵ *Fakultät Physik, Technische Universität Dortmund, Dortmund, Germany*
- ¹⁶ *Max-Planck-Institut für Kernphysik (MPIK), Heidelberg, Germany*
- ¹⁷ *Physikalisches Institut, Ruprecht-Karls-Universität Heidelberg, Heidelberg, Germany*
- ¹⁸ *School of Physics, University College Dublin, Dublin, Ireland*
- ¹⁹ *INFN Sezione di Bari, Bari, Italy*
- ²⁰ *INFN Sezione di Bologna, Bologna, Italy*
- ²¹ *INFN Sezione di Ferrara, Ferrara, Italy*
- ²² *INFN Sezione di Firenze, Firenze, Italy*
- ²³ *INFN Laboratori Nazionali di Frascati, Frascati, Italy*
- ²⁴ *INFN Sezione di Genova, Genova, Italy*
- ²⁵ *INFN Sezione di Milano, Milano, Italy*
- ²⁶ *INFN Sezione di Milano-Bicocca, Milano, Italy*
- ²⁷ *INFN Sezione di Cagliari, Monserrato, Italy*
- ²⁸ *Università degli Studi di Padova, Università e INFN, Padova, Padova, Italy*
- ²⁹ *INFN Sezione di Pisa, Pisa, Italy*
- ³⁰ *INFN Sezione di Roma La Sapienza, Roma, Italy*
- ³¹ *INFN Sezione di Roma Tor Vergata, Roma, Italy*
- ³² *Nikhef National Institute for Subatomic Physics, Amsterdam, Netherlands*
- ³³ *Nikhef National Institute for Subatomic Physics and VU University Amsterdam, Amsterdam, Netherlands*
- ³⁴ *AGH - University of Science and Technology, Faculty of Physics and Applied Computer Science, Kraków, Poland*
- ³⁵ *Henryk Niewodniczanski Institute of Nuclear Physics Polish Academy of Sciences, Kraków, Poland*
- ³⁶ *National Center for Nuclear Research (NCBJ), Warsaw, Poland*
- ³⁷ *Horia Hulubei National Institute of Physics and Nuclear Engineering, Bucharest-Magurele, Romania*
- ³⁸ *Affiliated with an institute covered by a cooperation agreement with CERN*
- ³⁹ *ICCUB, Universitat de Barcelona, Barcelona, Spain*
- ⁴⁰ *Instituto Galego de Física de Altas Enerxías (IGFAE), Universidade de Santiago de Compostela, Santiago de Compostela, Spain*
- ⁴¹ *Instituto de Física Corpuscular, Centro Mixto Universidad de Valencia - CSIC, Valencia, Spain*
- ⁴² *European Organization for Nuclear Research (CERN), Geneva, Switzerland*
- ⁴³ *Institute of Physics, Ecole Polytechnique Fédérale de Lausanne (EPFL), Lausanne, Switzerland*
- ⁴⁴ *Physik-Institut, Universität Zürich, Zürich, Switzerland*
- ⁴⁵ *NSC Kharkiv Institute of Physics and Technology (NSC KIPT), Kharkiv, Ukraine*
- ⁴⁶ *Institute for Nuclear Research of the National Academy of Sciences (KINR), Kyiv, Ukraine*
- ⁴⁷ *University of Birmingham, Birmingham, United Kingdom*
- ⁴⁸ *H.H. Wills Physics Laboratory, University of Bristol, Bristol, United Kingdom*
- ⁴⁹ *Cavendish Laboratory, University of Cambridge, Cambridge, United Kingdom*
- ⁵⁰ *Department of Physics, University of Warwick, Coventry, United Kingdom*

- ⁵¹ STFC Rutherford Appleton Laboratory, Didcot, United Kingdom
⁵² School of Physics and Astronomy, University of Edinburgh, Edinburgh, United Kingdom
⁵³ School of Physics and Astronomy, University of Glasgow, Glasgow, United Kingdom
⁵⁴ Oliver Lodge Laboratory, University of Liverpool, Liverpool, United Kingdom
⁵⁵ Imperial College London, London, United Kingdom
⁵⁶ Department of Physics and Astronomy, University of Manchester, Manchester, United Kingdom
⁵⁷ Department of Physics, University of Oxford, Oxford, United Kingdom
⁵⁸ Massachusetts Institute of Technology, Cambridge, MA, United States
⁵⁹ University of Cincinnati, Cincinnati, OH, United States
⁶⁰ University of Maryland, College Park, MD, United States
⁶¹ Los Alamos National Laboratory (LANL), Los Alamos, NM, United States
⁶² Syracuse University, Syracuse, NY, United States
⁶³ School of Physics and Astronomy, Monash University, Melbourne, Australia, associated to ⁵⁰
⁶⁴ Pontifícia Universidade Católica do Rio de Janeiro (PUC-Rio), Rio de Janeiro, Brazil, associated to ²
⁶⁵ Physics and Micro Electronic College, Hunan University, Changsha City, China, associated to ⁷
⁶⁶ Guangdong Provincial Key Laboratory of Nuclear Science, Guangdong-Hong Kong Joint Laboratory of Quantum Matter, Institute of Quantum Matter, South China Normal University, Guangzhou, China, associated to ³
⁶⁷ School of Physics and Technology, Wuhan University, Wuhan, China, associated to ³
⁶⁸ Departamento de Física , Universidad Nacional de Colombia, Bogota, Colombia, associated to ¹³
⁶⁹ Universität Bonn - Helmholtz-Institut für Strahlen und Kernphysik, Bonn, Germany, associated to ¹⁷
⁷⁰ Eotvos Lorand University, Budapest, Hungary, associated to ⁴²
⁷¹ INFN Sezione di Perugia, Perugia, Italy, associated to ²¹
⁷² Van Swinderen Institute, University of Groningen, Groningen, Netherlands, associated to ³²
⁷³ Universiteit Maastricht, Maastricht, Netherlands, associated to ³²
⁷⁴ DS4DS, La Salle, Universitat Ramon Llull, Barcelona, Spain, associated to ³⁹
⁷⁵ Department of Physics and Astronomy, Uppsala University, Uppsala, Sweden, associated to ⁵³
⁷⁶ University of Michigan, Ann Arbor, MI, United States, associated to ⁶²

^a Universidade Federal do Triângulo Mineiro (UFTM), Uberaba-MG, Brazil

^b Central South U., Changsha, China

^c Hangzhou Institute for Advanced Study, UCAS, Hangzhou, China

^d Excellence Cluster ORIGINS, Munich, Germany

^e Universidad Nacional Autónoma de Honduras, Tegucigalpa, Honduras

^f Università di Bari, Bari, Italy

^g Università di Bologna, Bologna, Italy

^h Università di Cagliari, Cagliari, Italy

ⁱ Università di Ferrara, Ferrara, Italy

^j Università di Firenze, Firenze, Italy

^k Università di Genova, Genova, Italy

^l Università degli Studi di Milano, Milano, Italy

^m Università di Milano Bicocca, Milano, Italy

ⁿ Università di Modena e Reggio Emilia, Modena, Italy

^o Università di Padova, Padova, Italy

^p Università di Perugia, Perugia, Italy

^q Scuola Normale Superiore, Pisa, Italy

^r Università di Pisa, Pisa, Italy

^s Università della Basilicata, Potenza, Italy

^t Università di Roma Tor Vergata, Roma, Italy

^u Università di Siena, Siena, Italy

^v Università di Urbino, Urbino, Italy

† Deceased